Molecular Cell

Article

Oncogenic K-Ras suppresses global miRNA function

Graphical abstract

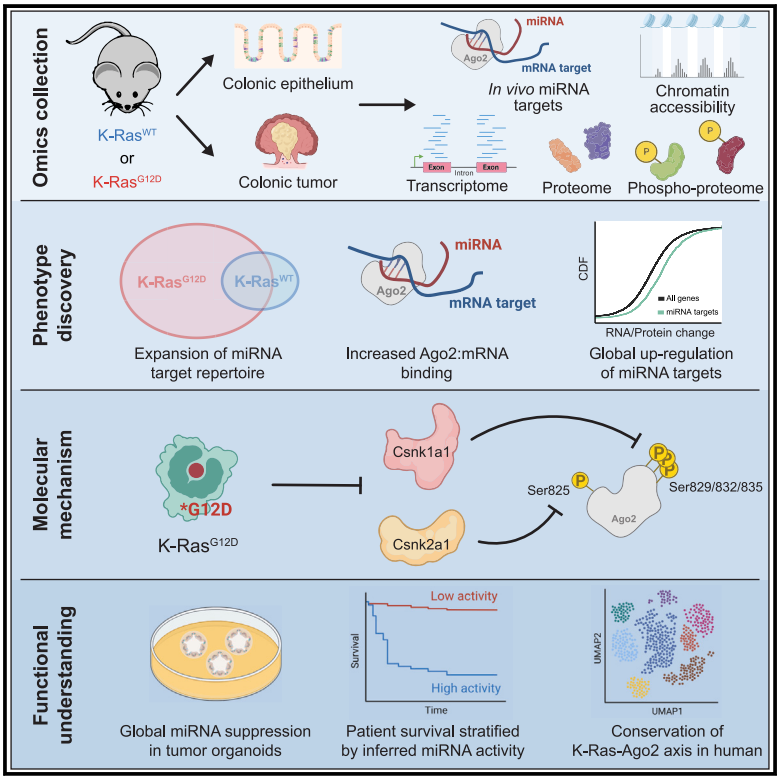

Highlights

- Oncogenic K-Ras induces global de-repression of physiological miRNA targets *in vivo*
- K-Ras^{G12D} enhances Ago2:mRNA binding, likely through Ago2 hypo-phosphorylation
- K-Ras^{G12D} transcriptionally suppresses Csnk1a1 and Csnk2a1 expression/activities
- Csnk1a1 and Csnk2a1 may hierarchically cooperate in their phosphorylation of Ago2

Authors

Bing Shui, Tyler S. Beyett, Zhengyi Chen, ..., Ken S. Lau, Andrea Ventura, Kevin M. Haigis

Correspondence

kevin_haigis@dfci.harvard.edu

In brief

Shui et al. report the *in vivo* de-repression of global miRNA targets induced by the oncogenic K-Ras (K-Ras^{G12D}) that is paradoxically accompanied by the enhanced Ago2:mRNA binding. Integrating *in vivo* modeling with omics network analysis, they mechanistically connect the K-Ras oncogene to the dysregulation of hundreds of downstream RNA/proteins.

Shui et al., 2023, Molecular Cell *83*, 2509–2523
July 20, 2023
https://doi.org/10.1016/j.molcel.2023.06.008

CellPress

Molecular Cell

CellPress

Article

Oncogenic K-Ras suppresses global miRNA function

Bing Shui,[1,2,3] Tyler S. Beyett,[1,4] Zhengyi Chen,[6,7] Xiaoyi Li,[8,9] Gaspare La Rocca,[8] William M. Gazlay,[1,4,5] Michael J. Eck,[1,4] Ken S. Lau,[6,7] Andrea Ventura,[8] and Kevin M. Haigis[1,2,10,11,*]

[1]Department of Cancer Biology, Dana Farber Cancer Institute, Boston, MA 02215, USA
[2]Department of Medicine, Brigham & Women's Hospital and Harvard Medical School, Boston, MA 02215, USA
[3]Program in Biological and Biomedical Sciences, Division of Medicine, Harvard Medical School, Boston, MA 02115, USA
[4]Department of Biological Chemistry and Molecular Pharmacology, Harvard Medical School, Boston, MA 02115, USA
[5]Department of Chemistry, University of Massachusetts Boston, Boston, MA 02125, USA
[6]Epithelial Biology Center, Vanderbilt University Medical Center, Nashville, TN 37232, USA
[7]Department of Cell and Developmental Biology, Chemical and Physical Biology Program, Vanderbilt University School of Medicine, Nashville, TN 37232, USA
[8]Cancer Biology and Genetics Program, Memorial Sloan Kettering Cancer Center, New York, NY 10065, USA
[9]Louis V. Gerstner Jr. Graduate School of Biomedical Sciences, Memorial Sloan Kettering Cancer Center, New York, NY 10065, USA
[10]Harvard Digestive Disease Center, Harvard Medical School, Boston, MA 02215, USA
[11]Lead contact
*Correspondence: kevin_haigis@dfci.harvard.edu
https://doi.org/10.1016/j.molcel.2023.06.008

SUMMARY

K-Ras frequently acquires gain-of-function mutations (K-Ras^{G12D} being the most common) that trigger significant transcriptomic and proteomic changes to drive tumorigenesis. Nevertheless, oncogenic K-Ras-induced dysregulation of post-transcriptional regulators such as microRNAs (miRNAs) during oncogenesis is poorly understood. Here, we report that K-Ras^{G12D} promotes global suppression of miRNA activity, resulting in the upregulation of hundreds of targets. We constructed a comprehensive profile of physiological miRNA targets in mouse colonic epithelium and tumors expressing K-Ras^{G12D} using Halo-enhanced Argonaute pull-down. Combining this with parallel datasets of chromatin accessibility, transcriptome, and proteome, we uncovered that K-Ras^{G12D} suppressed the expression of Csnk1a1 and Csnk2a1, subsequently decreasing Ago2 phosphorylation at Ser825/829/832/835. Hypo-phosphorylated Ago2 increased binding to mRNAs while reducing its activity to repress miRNA targets. Our findings connect a potent regulatory mechanism of global miRNA activity to K-Ras in a pathophysiological context and provide a mechanistic link between oncogenic K-Ras and the post-transcriptional upregulation of miRNA targets.

INTRODUCTION

Ras proteins are small GTPases that can be mutational activated to drive oncogenesis in many tissues. Most notably, glycine 12 substitutions of K-Ras are detected in ~80% of pancreatic ductal adenocarcinomas (PDAC), ~30% of non-small cell lung cancers (NSCLCs), and ~23% of colorectal cancers (CRC), with glycine to aspartic acid (G12D) being the common mutation.[1] The K-Ras^{G12D} oncoprotein hyperactivates canonical Ras signaling and its direct physiological impact in several tissue contexts has been extensively characterized over the past two decades using genetically engineered mouse models.[2–7] Despite what we know about oncogenic effects of K-Ras^{G12D} *in vivo*, it remains unclear at a mechanistic level how it alters the cellular signaling network to affect homeostasis.

Regulation of protein levels can be achieved transcriptionally, post-transcriptionally, and post-translationally. miRNAs are short, noncoding RNAs (~21 nt) that serve as post-transcriptional regulators with a large repertoire of targets.[8] To further elucidate the dramatic disturbance of the proteomic landscape upon expression of oncogenic K-Ras^{G12D} in the colonic epithelium and tumors, we considered microRNAs (miRNAs) as potential mediators of downstream Ras signaling. Canonical miRNAs function by binding to Argonaute proteins (AGO1–4), with AGO2 being the dominant form.[9] Serving as guides, miRNAs direct AGOs to mRNA transcripts through nucleotide homology, canonically to the 3′ UTR region of the transcript. Suppression of target mRNA translation is achieved through subsequent recruitment of TNRC6 and other members of the RNA-induced silencing complex (RISC).[8,10,11] Additionally, RISC can also destabilize target mRNAs through recruitment of decapping and deadenylating proteins.[12,13] miRNA targeting of mRNA requires only imperfect reverse complementarity of its seed sequence (nucleotide 2–7), rending a broad targeting process.[14] Therefore, each miRNA has hundreds of potential targets, making it a potent regulator of both transcriptomic and proteomic landscapes.

The interplay between K-RAS and individual miRNAs has long been established. For example, K-RAS is a target of let-7, one of the first miRNAs identified[15,16] and the miR181ab1 cluster was recently shown to be critical for K-RAS driven oncogenesis in lung and pancreas.[17] Nevertheless, systematic characterization of the downstream impacts of oncogenic K-RAS on miRNA function has been largely limited to *in vitro* systems and heavily dependent on miRNA target prediction algorithms such as TargetScan, miRanda, and PicTar.[14,18,19] These computational approaches survey the genome for potential miRNA-binding sites, yet they are limited by our incomplete understanding of rules that govern miRNA targeting. Moreover, several recent reports have highlighted tissue- and context-specific functions of miRNAs,[20,21] which further underscores the importance of studying physiological miRNA-mRNA interactions *in vivo*. This is made possible by recent developments in crosslinking immunoprecipitation coupled with next-generation sequencing (CLIP-seq), allowing for identification of physiological miRNA targets.[22–25] Using Halo-enhanced Argonaute pull-down (HEAP), a new approach that enabled high-resolution identifications of miRNA targets *in vivo*,[26] we established a comprehensive profile of active and physiological miRNA targets in the mouse colonic epithelium and colonic tumors, both in the presence and absence of oncogenic K-Ras, enabling the study of a single mutation's impact on the miRNA activity landscape. Furthermore, by integrating miRNA target profile with analysis of the transcriptome, proteome, and chromatin accessibility landscape, we have mechanistically characterized the global suppression of miRNA function induced by K-Ras^{G12D}.

RESULTS

Global profiling of miRNA-binding sites in colonic epithelium and tumors

Our initial goal was to determine the physiological miRNA target repertoire in mouse colonic epithelium and tumors, with and without endogenous expression of oncogenic K-Ras. We generated *Fabp1-Cre ; Ago2$^{LSL-Halo/+}$; Kras$^{LSL-G12D/+}$* mice for colonic epithelium-specific expression of K-Ras^{G12D} and Halo-tagged Ago2.[3,26,27] For the inducible model of CRC, we utilized *Villin-Cre^{ERT2} ; Ago2$^{LSL-Halo/+}$; Apc$^{fl/fl}$; Kras$^{LSL-G12D/+}$* mice.[28,29] Tumor induction in these animals can be rapidly achieved via enema of 4-hydroxytamoxifen (4-OHT), leading to the tumor-initiating loss of Apc and endogenous expression of Halo-Ago2 and K-Ras^{G12D} (Figures 1A and 1B). Despite endogenous expression, K-Ras levels appeared elevated in tissues expressing K-Ras^{G12D} (Figure 1B). This could potentially be attributed to the increased stability of K-Ras^{G12D} from elevated Ras-GTP levels and frequent binding to effectors.

To study the influence of oncogenic K-Ras on miRNAs, we validated three properties of our mouse models. First, we measured activation of the mitogen-activated protein kinase (MAPK) pathway, canonically downstream of K-Ras. We found that K-Ras^{G12D} expression enhanced MAPK signaling in tissues, with the elevation of activating phosphorylation of Mek (Ser217/221) and Erk (Thr202/Tyr204) (Figure S1A). Second, we found that mice harboring colonic tumors expressing K-Ras^{G12D} exhibited shorter survival relative to those with K-Ras^{WT} tumors (Figure S1B), corroborating the relatively poor prognosis of patients with K-Ras mutant CRCs.[6,30] Finally, we found that Halo-Ago2 expression did not interfere with K-Ras^{G12D}-associated phenotypes in the colon and distal ileum, including increased height of the crypts and Ki67+ proliferating zone, upregulated p-Erk (Thr202/Tyr204), and loss of Paneth cells (Figures S1C and S1D).[6,31]

We next performed HEAP to examine the landscape of miRNA activity and abundance, revealing distinct miRNA target profiles in tissues with and without K-Ras^{G12D} (Figure S1E). By applying Clipanalyze (https://bitbucket.org/leslielab/clipanalyze), we identified 1,283/5,109 active miRNA-binding sites in colonic epithelium and 2,186/7,569 binding sites in colonic tumor expressing K-Ras^{WT}/K-Ras^{G12D}. In all conditions, ~50% of peaks were present in the 3′ UTR of genes and ~30%–40% in the coding sequence (CDS) (Figures 1C and S1F). The distribution of target sites in these various genomic locations was consistent with profiles described previously.[26,32] We associated miRNA families with HEAP peaks by searching for Kmer (8-mer, 7-mer, and 6-mer) matches to mature miRNA seed sequences. The abundance of Ago2-bound miRNAs positively correlated with the number of associated peaks, suggesting that more abundant miRNAs likely have higher binding activities (Figures 1D and S1G). Among broadly conserved miRNA families, we found let-7-5p, miR-194-5p, and miR-200/429-3p to be among the most active miRNAs in the colonic epithelium and tumor. We benchmarked HEAP targets from mice with computationally predicted miRNA target pairings in human from the TargetScan database[14] and observed significant enrichment, suggesting considerable conservation of miRNA:-target matching between mouse and human (Figure 1E).

To confirm the physiological relevance of the identified miRNA targets, we utilized a mouse strain carrying a doxycycline-inducible T6B-YFP transgene. T6B is a small peptide that suppresses global miRNA function by disrupting the Ago:Tnrc6 interaction in the RISC complex.[21] T6B expression in mouse colon induced drastic changes in the transcriptome with transcript levels of HEAP target genes preferentially upregulated upon T6B expression, suggesting that the targets identified by the HEAP were functional (Figure S1H). We then measured gene expression changes associated with each miRNA family using the parametric analysis of gene-set enrichment (PAGE)[33] and found that gene targets of more abundant miRNA families experienced more significant de-repression upon T6B-mediated inhibition of miRNA function (Figure 1F). In conclusion, we have established a physiological miRNA target map for colonic epithelium and tumors expressing K-Ras^{WT} and K-Ras^{G12D}, allowing for the granular study of the impact of a single gene mutation on miRNA activity *in vivo* (Data S1).

K-Ras^{G12D} expands functional miRNA target repertoire with global de-repression

We next investigated the impact of K-Ras^{G12D} on the miRNA target landscape. We observed a major overlap between miRNA targets identified in colonic tissues with and without K-Ras^{G12D}. Strikingly, both colonic epithelium and tumors expressing K-Ras^{G12D} exhibited a significant expansion of their miRNA target repertoire (Figures 2Aand S2A), prompting the hypothesis that

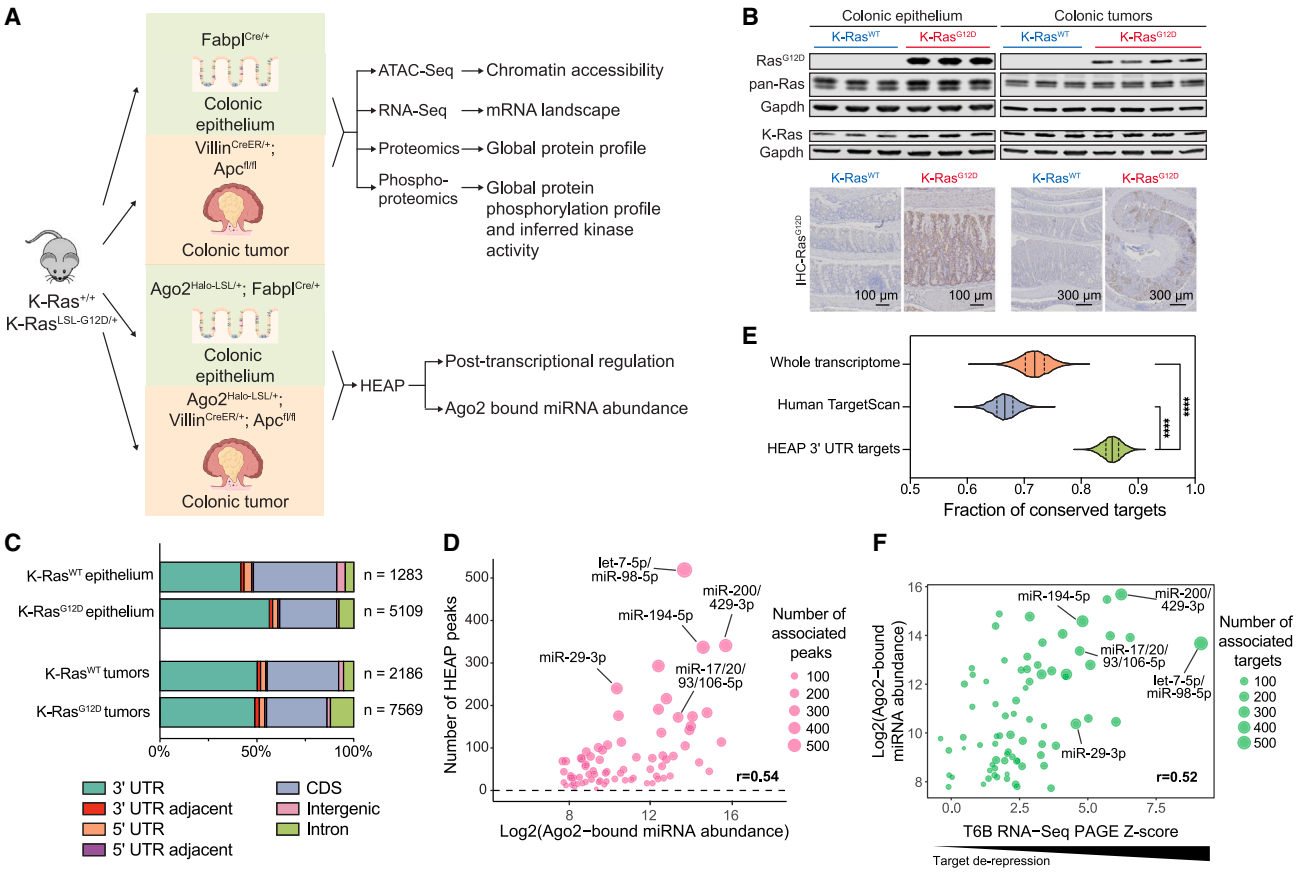

Figure 1. Global profiling of miRNA-binding sites in colonic epithelium and tumors

(A) Schematic of mouse models and data collection for this study.

(B) Endogenous expression of oncogenic K-Ras^{G12D} in mouse colonic epithelium and tumors. Pan-Ras and K-Ras levels were also examined. Scale bars: 100 μm—colonic epithelium, 300 μm—colonic tumors.

(C) Genomic distribution of physiological miRNA target sites identified by HEAP in colons ± K-Ras^{G12D}. CDS, coding sequence; 5′ UTR, 5′ untranslated region; 3′ UTR, 3′ untranslated region.

(D) Positive correlation between Ago2-bound abundance and the number of associated targets for each miRNA family in colonic epithelium. Each dot represents an individual miRNA family. Pearson correlation coefficient r = 0.54.

(E) Conservation of HEAP miRNA targets in human. Fraction of randomly sampled targets from each set that are predicted to be targets of active miRNA families in the TargetScan human database (detailed in the STAR Methods section). **** $p < 0.0001$ by Šídák's multiple comparisons test.

(F) De-repression of HEAP-identified miRNA targets upon T6B-induced global miRNA suppression in the mouse colon. T6B RNA PAGE *Z* score positively correlates with Ago2-bound miRNA abundance. PAGE *Z* score calculation is detailed in the STAR Methods section. Each dot represents an individual miRNA family. Higher PAGE *Z* score indicates stronger de-repression of miRNA targets in mouse colon expressing miRNA suppressor T6B. Pearson correlation coefficient r = 0.52.

See also Figure S1 and Data S1 for the HEAP-identified miRNA targets.

hyperactivated K-Ras might affect miRNA function globally. Expecting that a global dysregulation of miRNA function would broadly influence RNA and protein expression, we collected transcriptomic, proteomic, and phospho-proteomic data using tissues from the same models subjected to HEAP (Data S2).[34] The expression of K-Ras^{G12D} induced considerable changes in both colonic epithelium and tumors, each with thousands of transcripts/proteins dysregulated (RNA: adjusted p value < 0.05; protein: $p < 0.05$ and $q < 0.1$) (Figures S2B, S2C, and S2H). While the transcriptomic and proteomic datasets as a whole exhibited moderate correlation, there was minimal overlap between significantly differentially expressed mRNAs and proteins (Figures S2D–S2G). The lack of correlating changes between RNA and protein suggested potential post-transcriptional regulation induced by oncogenic K-Ras.

Among HEAP targets, 4,271 and 5,543 peaks were specific to K-Ras^{G12D}-expressing colonic epithelium and tumors (Figures 2A and S2A). We expected that genes targeted by miRNA specifically in K-Ras^{G12D} tissues would exhibit decreased RNA and protein levels in tissues expressing mutant K-Ras. Surprisingly, K-Ras^{G12D}-specific miRNA targets were enriched for upregulated RNA and proteins (Figures 2B, 2C, S2I, and S2J, $p < 0.0001$, Fisher's exact test). Indeed, more than 40% of K-Ras^{G12D}-specific miRNA targets exhibited

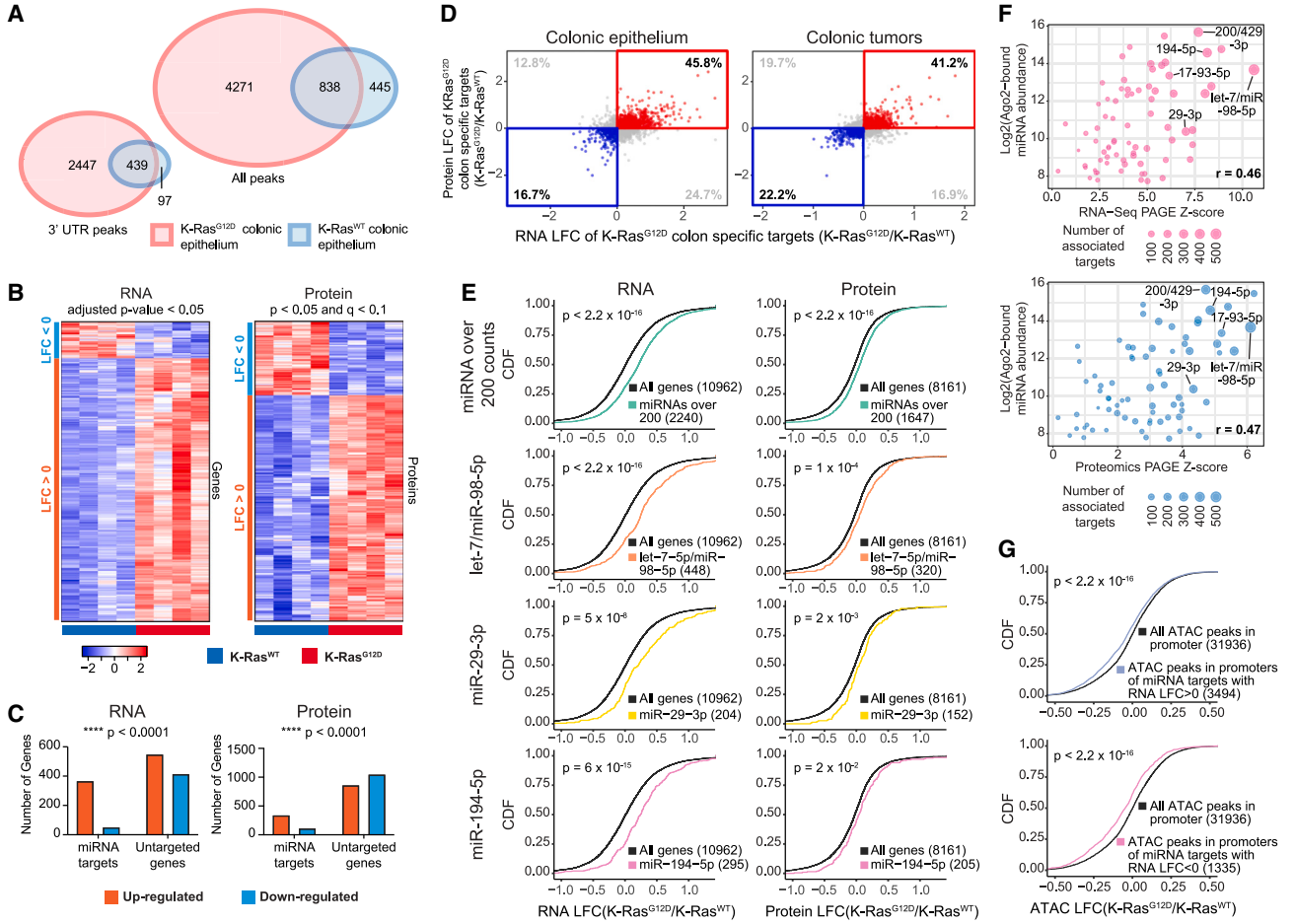

Figure 2. K-Ras^{G12D} expands functional miRNA target repertoire with global de-repression

(A) Overlap of miRNA target sites in K-Ras^{WT} and K-Ras^{G12D} colonic epithelium.

(B) Heatmap of significantly dysregulated RNA and protein of K-Ras^{G12D}-specific miRNA targets in the colonic epithelium.

(C) Enrichment of significantly upregulated RNA and proteins of K-Ras^{G12D}-specific miRNA targets compared with those of untargeted genes in colonic epithelium. **** $p < 0.0001$ by Fisher's exact test.

(D) Heatmap of significantly dysregulated RNA and protein of K-Ras^{G12D}-specific miRNA targets in the colonic epithelium.

(E) Cumulative distribution function (CDF) plot of RNA and protein changes for targets of miRNAs over 200 counts (let-7-5p/miR-98-5p, miR-29-3p, and miR-194-5p) in mouse colonic epithelium. Log fold change (LFC) was calculated as K-Ras^{G12D} vs. K-Ras^{WT}. p value by two-sided Kolmogorov-Smirnov test.

(F) Global upregulation of miRNA targets upon K-Ras^{G12D} expression in the mouse colon. Ago2-bound miRNA abundance positively correlates with RNA/protein PAGE *Z* score. Each dot represents an individual miRNA family. Higher PAGE *Z* score indicates stronger de-repression of miRNA target RNA/protein in mouse colon expressing K-Ras^{G12D}. Pearson correlation coefficient r = 0.46 (RNA) and 0.47 (protein).

(G) CDF plots of transcription start site (TSS) chromatin accessibility changes in promoters of miRNA target genes with RNA LFC > 0 or < 0 in mouse colonic epithelium from ATAC-seq. Chromatin accessibility change (ATAC peak LFC) was calculated as K-Ras^{G12D} vs. K-Ras^{WT}. p value by two-sided Kolmogorov-Smirnov test.

See also Figure S2 and Data S2 for profiled RNA, protein, and chromatin accessibility.

upregulation in both RNA and protein (Figure 2D). This prompted us to consider whether hyperactive K-Ras could promote, rather than suppress, the expression of miRNA targets. Examination of the RNA and protein expression changes in tissues expressing K-Ras^{G12D} demonstrated that gene targets of almost all miRNA families were globally upregulated (Figures 2E and S2K). We then investigated whether the upregulation of miRNA target RNA and protein was influenced by their associated targeting miRNA. PAGE analysis indicated that the target genes of highly abundant miRNA families were preferentially upregulated both at the RNA and protein levels upon oncogenic K-Ras expression (Figures 2F and S2L). Drawing similarities between this observation in K-Ras^{G12D} tissues and the T6B-induced transcriptomic changes, we hypothesized that the de-repression of miRNA targets could stem from global dysregulation of miRNAs rather than that of individual miRNAs.

It remained a formal possibility that the paradoxically increased expression of miRNA targets in K-Ras mutant tissue might result from strong transcriptional upregulation that overcomes traditional miRNA-mediated downregulation. To address

this possibility, we performed ATAC-seq (assay for transposase-accessible chromatin with sequencing) to profile the chromatin accessibility landscape of colonic tissues expressing K-Ras^{WT} and K-Ras^{G12D}, as chromatin accessibility at gene promoters have been widely used as to estimate transcriptional activity.[35,36] As expected, tissues ± oncogenic K-Ras displayed distinctive profiles (Figure S2M). Integration of the chromatin status with the transcriptomic data revealed that genes with significantly downregulated RNA preferentially exhibited downregulated transcription in tissues with K-Ras^{G12D} (Figure S2N), demonstrating that lower rates of transcription were the main determinant of lower gene expression. We then investigated if chromatin accessibility alone was sufficient to predict transcriptomic changes. While genes with more accessible promoters increased in RNA, genes with suppressed ATAC signal at the promoter did not necessarily decrease in RNA (Figure S2O). This observation suggests that a potential post-transcriptional regulation program could overcome the transcriptional suppression of many genes to result in their stable expression or upregulation, corroborating our observed global increase in expression of miRNA targets. Most importantly, miRNA targets with both up- and downregulated RNAs exhibited significant suppression of transcription (Figures 2G and S2P), undermining the likelihood of transcriptional de-repression of miRNA targets. Taken together, these data suggest that the hyperactivation of K-Ras induces global de-repression of miRNA targets that is dependent on miRNA expression level, but independent of a given target's transcriptional status.

Active miRNA families are conserved across mutational and histological contexts

Our studies thus far suggest a contradictory role for K-Ras in regulating miRNA function, with its hyperactivation expanding the miRNA target repertoire while simultaneously de-repressing miRNA target RNA and proteins. To resolve this apparent conflict, we first set out to examine whether specific miRNAs were differentially active in K-Ras^{WT} or K-Ras^{G12D} tissues. To infer miRNA activity from the abundance of associated target sites, we performed HOMER (hypergeometric optimization of motif enrichment) motif enrichment in condition-specific HEAP peaks (peaks only identified in K-Ras^{WT} or K-Ras^{G12D} samples). Surprisingly, we identified a largely consistent cohort of miRNAs to be highly active in the colon across various mutational and histological states (K-Ras^{WT} vs. K-Ras^{G12D}, epithelium vs. tumor) (Figures 3A and S3A). Among these, *let-7-5p/miR-98-5p*, *miR-29-3p*, *miR-200/429-3p*, and *miR-17∼93-5p* were well-characterized miRNA families, with roles in both homeostatic and pathological conditions.[16,32,37–40] Functional enrichment of their targets with KEGG (Kyoto Encyclopedia of Genes and Genomes) underscored their physiological importance, with many critical functional terms enriched as miRNA targets, including mTOR signaling, cAMP signaling, PI3K-AKT signaling, MAPK signaling, and Ras signaling pathway itself (Figures S3B and S3C). The motif of *miR-194-5p*, a relatively understudied miRNA, was also highly enriched across all conditions, suggesting that *miR-194-5p* might play a crucial role *in vivo* that remains to be elucidated.

While capturing target mRNA transcripts, HEAP also profiles the miRNAs that are bound to Ago2.[26] Accordingly, we next examined whether perturbation of active miRNA expression by oncogenic K-Ras could contribute to the expanded miRNA target repertoire or the global upregulation of miRNA targets. isomiR profiles remained consistent upon oncogenic K-Ras expression, with 3′ trimming being the dominant isoform (Figure S3D). Hierarchical clustering revealed distinct Ago2-bound miRNA abundance profiles of K-Ras^{WT}- and K-Ras^{G12D}-expressing tissues (Figure S3E), with several miRNAs that were previously shown to be regulated by K-Ras signaling exhibiting dysregulated abundance, including *miR-30b-5p*, *miR-210-3p*, *miR-127-3p*, and *miR-137-3p* (Figures 3B and S3F).[41,42] However, the highly abundant/active miRNA families (*let-7-5p/miR-98-5p*, *miR-29-3p*, *miR-200/429-3p*, and *miR-17∼93-5p*, *miR-194-5p*) remained largely unaffected, with log fold changes (LFCs) around 0, in K-Ras^{G12D} tissues, corroborating their stable cytoplasmic miRNA levels across conditions (Figures 3C, 3D, and S3G). Accordingly, most HEAP targets were associated with miRNA families of stable Ago2-bound abundance, undermining the likelihood of a miRNA abundance-driven phenotype (Figure S3H).

Integrating our identification of Ago2-bound miRNAs with our HOMER motif enrichment analysis, a conserved cohort of active miRNAs emerged disregarding the mutational and histological contexts in the colon and remained relatively stable upon K-Ras hyperactivation both in their Ago2-bound level and their mRNA targeting activity. Thus, changes in miRNA levels are unlikely to underly the conflicting effect of K-Ras^{G12D} on miRNA targeting and miRNA target de-repression.

Oncogenic K-Ras-enhances Ago2:mRNA binding without RISC perturbation

Given the stable profile of Ago2-bound miRNAs, we next turned to the interaction between Ago2 and target mRNAs. Differential binding affinity analysis was performed using read counts within HEAP peaks (miRNA target sites), with higher read counts indicating stronger binding between Ago2 and the target mRNA. Read counts outside of the peaks were considered non-specifically bound RNA and were used for global normalization. For all miRNA families, we observed increased binding between Ago2 and their target mRNAs in tissues expressing K-Ras^{G12D} (mean peak signal LFC > 0), while their Ago2-bound miRNA abundance remained stable (Figures 4A and S4A). Further investigation of individual miRNA families demonstrated significantly enhanced target binding for all major miRNA families in tissues expressing K-Ras^{G12D} (Figures 4B and S4B). To understand if the change was driven by a few dominant peaks or a global shift in Ago2:mRNA-binding affinity, we examined signal changes of all peaks and peaks associated with several active miRNA families. We found that that the majority of HEAP peaks demonstrated increased binding signal in colonic tissues expressing K-Ras^{G12D} (Figures 4C, S4C, and S4D), suggesting a non-discriminatory increase in Ago2:mRNA-binding affinity. Again, we considered the possibility that the increase of Ago2-bound mRNA was a passive effect of an overall increase in target transcripts. Therefore, we selected miRNA target genes with increased, stable, or decreased RNA/protein in the K-Ras^{G12D} colon. qPCR on target mRNA pulled down with Halo-Ago2 in colonic epithelium and tumors showed that significantly more

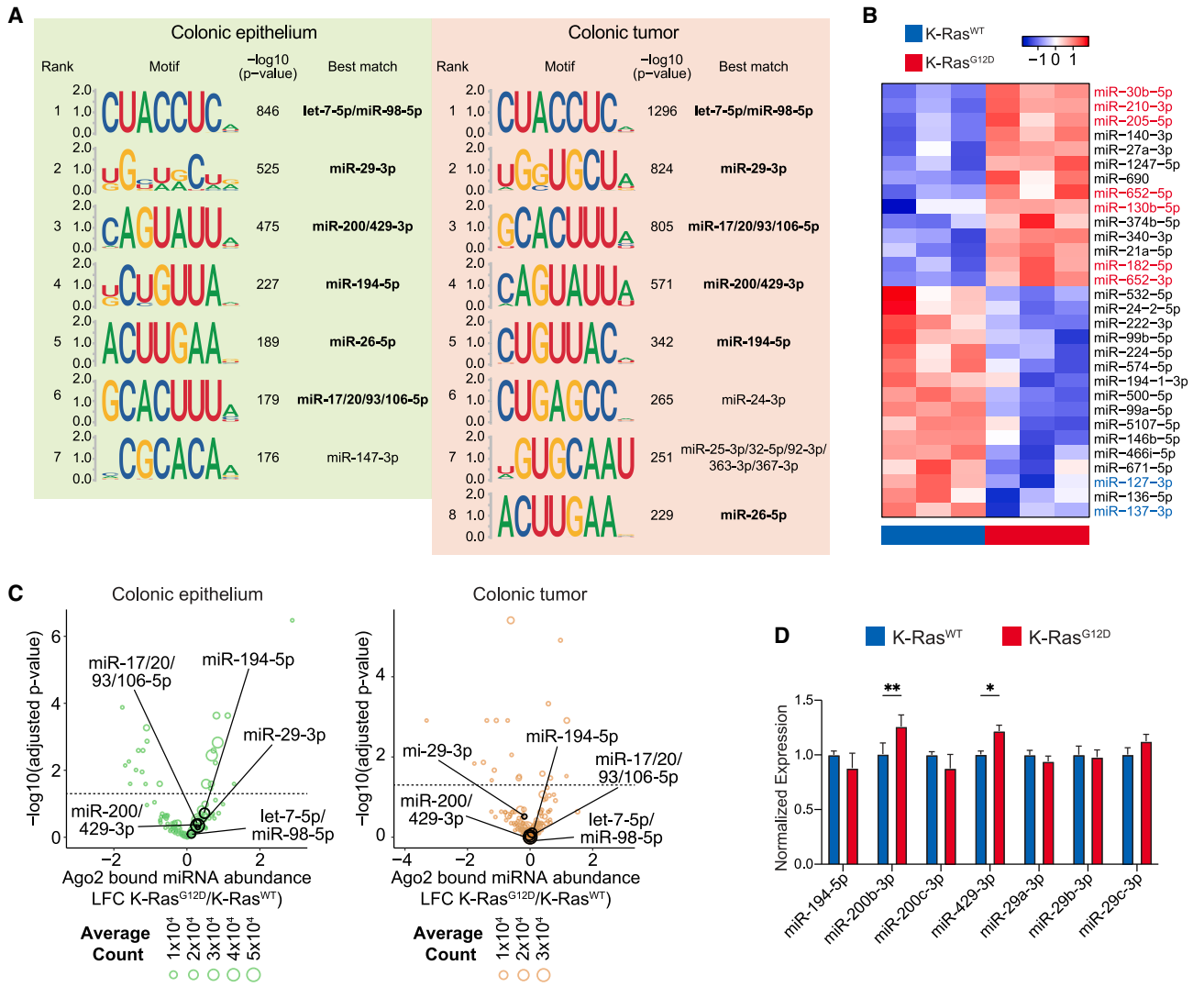

Figure 3. Active miRNA families are conserved across mutational and histological contexts

(A) Top differentially enriched 8-mers in colonic epithelium and tumors from merged HEAP target sites by the HOMER *de novo* motif enrichment algorithm. miRNA families whose seed sequences are complementary to these motifs are annotated.

(B) Heatmap of significantly dysregulated Ago2-bound miRNAs in HEAP from K-Ras^{G12D} expressing colon. miRNAs highlighted in blue (decrease) and red (increase) have previously been connected to K-Ras dysregulation. Adjusted p value < 0.05 by Wald test with Benjamini-Hochberg correction. Scale bar represents *Z* score.

(C) Volcano plot of global Ago2-bound miRNA abundance changes in colonic epithelium and tumors ± K-Ras^{G12D}. LFC is calculated as K-Ras^{G12D} vs. K-Ras^{WT}. Highly active and conserved miRNA families are annotated.

(D) qPCR of highly active miRNAs (with most associated miRNA targets) in colonic epithelium ± K-Ras^{G12D}. ** $p < 0.005$, * $p < 0.05$ by two-way ANOVA followed by Šídák's multiple comparisons test.

See also Figure S3 and Data S2 for HEAP profiled miRNA.

target mRNA associated with Ago2 in tissues expressing oncogenic K-Ras, independent of changes in their overall RNA/protein levels (Figures 4D and S4E).

Given the global shift in Ago2:mRNA binding, we asked whether oncogenic K-Ras could impact the functional status of the RISC, a protein complex critical for miRNA function. Argonaute proteins and TNRC6 family members are the primary components of RISC, with Ago2 being the dominant species.[9] Upon Ago2 binding to the target transcripts, TNRC6 recruits other proteins such as CCR4-NOT complex and DDX6 to execute miRNA-induced gene suppression.[8] Therefore, we examined the levels and functional status of RISC in colonic tissues expressing K-Ras^{WT} or K-Ras^{G12D}. Ago2 levels remained stable upon oncogenic K-Ras expression *in vivo* (Figure S4F). To examine the degree of Ago2:Tnrc6a interaction, we performed Halo-Ago2 pull-down in colonic epithelium and tumors ± K-Ras^{G12D} and demonstrated that a consistent amount of Tnrc6a associated with Ago2 upon activation of K-Ras (Figures 4E, S4G, and

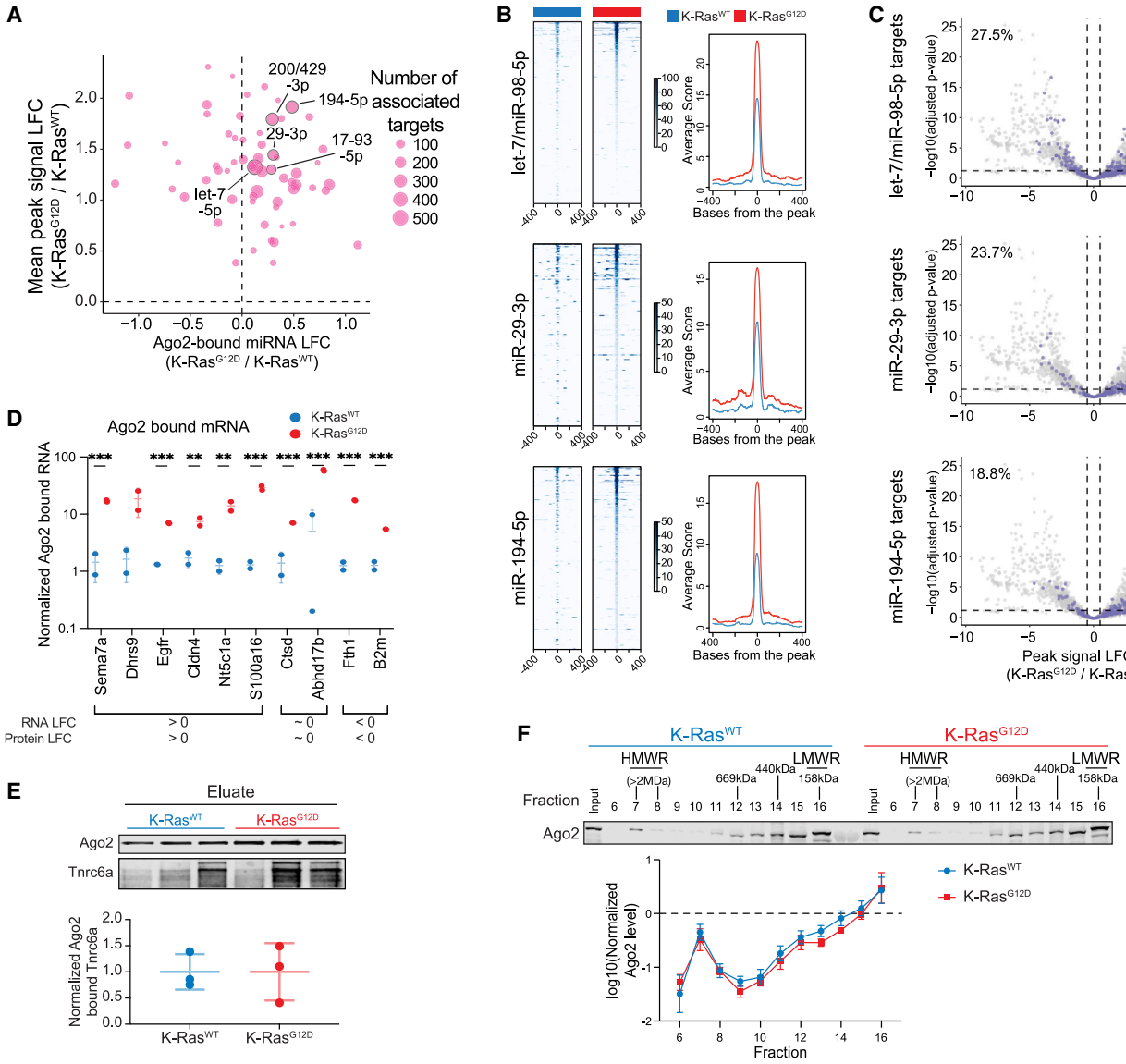

Figure 4. Oncogenic K-Ras enhances Ago2:mRNA binding without RISC perturbation

(A) Scatterplots correlating the LFC of Ago2-bound abundance for each miRNA family with the mean target-binding signal LFC of their targets in colonic epithelium. Each dot represents an individual miRNA family. Positive peak signal LFC indicates stronger Ago2:mRNA binding.

(B) Heatmap and histogram of peak signal in an 800-bp region surrounding HEAP peaks containing seed matches to let-7-5p/miR-98-5p, miR-29-3p, and miR-194-5p from colonic epithelium ± K-Ras^{G12D}. Scale bar represents normalized read counts.

(C) Volcano plots of global miRNA target peak signal change associated with let-7-5p/miR-98-5p, miR-29-3p, and miR-194-5p in colonic epithelium ± K-Ras^{G12D}. Each dot represents a HEAP target site, with purple color highlighting target sites associated with specified miRNA family. Peak signal LFC denotes the increase/decrease of miRNA target-binding signal detected by HEAP. Percentages of highlighted peaks with LFC above or below 0 are annotated.

(D) Halo-Ago2 pull-down followed by qPCR for mRNA transcripts bound to Ago2 in mouse colonic epithelium. Error bars represent ±SD, * $p < 0.1$. ** $p < 0.05$, *** < 0.01 by multiple unpaired t test.

(E) Anti-HaloTag pull-down of Halo-Ago2 in colon ± K-Ras^{G12D} to examine Ago2:Tnrc6a association. Error bars represent ±SD.

(F) RISC fractionation of colonic tumor ± K-Ras^{G12D} to examine the distribution of Ago2 in functional HMWR and non-functional LMWR normalized to input Ago2. Error bars represent ±SD.

See also Figure S4.

S4H). Given that RISC is an intricate protein complex with many potential interactors, we further investigated native RISC status *in vivo*. La Rocca et al. have previously reported that cellular Ago2 is largely distributed between high molecular weight RISC (HMWR, >2 MDa) and low molecular weight RISC (LMWR) (~100 kDa, Ago2 monomer state), with HMWR being the functional form.[20] Using size-exclusion chromatography, we evaluated the distribution of Ago2 between the HMWR and

LMWR fractions and detected Ago2 in both fractions with comparable levels, regardless of K-Ras^{G12D} status (Figures 4F and S4I), suggesting that RISC assembly status did not vary significantly upon hyperactivation of K-Ras signaling. This observation contradicted a recent report that implicated mutant K-Ras in inhibition of RISC assembly through a direct K-Ras:Ago2 interaction.[43] Therefore, we set out to understand whether Ago2 binds WT or mutant K-Ras in the mouse colon. Nevertheless, we did not observe stable interaction between Halo-Ago2 and K-Ras^{WT} or K-Ras^{G12D} in either colonic epithelium or tumors (Figures S4J and S4K).

Altogether, we observed that the endogenous expression of oncogenic K-Ras in colonic tissues enhanced global Ago2:mRNA binding while sparing the RISC. The increased Ago2:mRNA affinity drives the observed expansion of miRNA target repertoire in the K-Ras^{G12D}-expressing tissues. Given the established role of miRNAs in gene suppression, the oncogenic K-Ras-induced increase in Ago2:mRNA binding is paradoxical to the observed global de-repression of miRNA targets in tissues expressing K-Ras^{G12D}.

K-Ras^{G12D} suppresses Csnk1a1/Csnk2a1, regulators of Ago2 activity

With the conflict between global miRNA target de-repression and increased Ago2:mRNA interaction unresolved, we next investigated the functional status of Ago2 itself. Ago2 activity is tightly regulated by its phosphorylation status. Phosphorylation of Ser387, Tyr393, and Tyr529 affect Ago2 activity through various mechanisms, including facilitating Ago2 localization to processing bodies,[44] repressing its endonucleolytic cleavage activity,[45] disrupting miRNA loading,[46] and hindering its interaction with Dicer.[47] Moreover, a conserved cluster of serine phosphorylation sites was recently reported on Ago2 at Ser824/828/831/834 (mouse Ago2 Ser825/829/832/835), phosphorylation of which hindered effective Ago2:mRNA binding.[48,49] Proper cycling of phosphorylation on these sites is essential for Ago2 function. Analogous to what we observed in colonic tissues expressing K-Ras^{G12D}, removal of these phosphorylations through serine to alanine substitutions led to increased Ago2:mRNA binding, expansion of miRNA target repertoire, and global de-repression of miRNA targets *in vitro* as a small pool of target transcripts sequestered most functional Ago2.[48] Furthermore, hypo-phosphorylation of this cluster (Ago2^{5XA}) had no impact on Ago2 distribution in HMWR/LMWR, while hyper-phosphorylation completely disrupted functional RISC, suggesting that these phosphorylations prevent RISC assembly (Figure S5A). Similar to Ago2 hypo-phosphorylation, increased Ago2:mRNA binding resulting from oncogenic K-Ras favored RNA transcripts with a longer half-life (Figure S5B).[48]

With K-Ras signaling being key to the tissue phospho-proteome, we hypothesized that hyperactive K-Ras suppressed Ago2 phosphorylation at Ser825/829/832/835, which would account for the paradoxical increase in Ago2:mRNA binding and global de-repression of miRNA targets in tissues expressing K-Ras^{G12D}. Ankrd52-Ppp6c was identified as the regulatory phosphatase and removal of its activity promotes hyper-phosphorylation of Ago2, rendering Ago2 non-functional due to its inability to bind mRNA.[48] Indeed, we found that genome-wide CRISPR knockout (KO) screens in human cancer cell lines (DepMap 21Q2 Public + Score, CERES) revealed strong positive co-dependency between AGO2 and ANKRD52/PPP6C (Figure S5C). Ankrd52 KO in mouse embryonic fibroblasts (MEFs) increased Ago2 phosphorylation at the Ser825/829 sites, as measured by mass spectrometry (MS) (Figures S5D and S5E), indicating conservation of this regulatory mechanism in mouse tissues. However, Ankrd52 and Ppp6c levels were unperturbed upon K-Ras^{G12D} expression in mouse tissues, indicating that the dephosphorylation machinery likely remained stable (Figure S5F).

Csnk1a1 was shown to phosphorylate Ser829/832/835 of Ago2 hierarchically, with Ser829 phosphorylation being the priming event.[48,50] However, the kinase governing Ser825 phosphorylation was not identified. We used two algorithms (Scansite 4.0 and Kinome Xplorer) to identify kinases that potentially target Ser825 of Ago2 and identified CK2 as a candidate.[51,52] CK2 is a tetrameric kinase composed of two catalytic subunits encoded by CSNK2A1 and CSNK2A2, and two regulatory subunits encoded by CSNK2B.[53] We performed *in vitro* phosphorylation using purified Csnk2a1 and Ago2 peptide (816–838) and detected phosphorylation of Ser825 (Figure S5G). We observed robust phosphorylation of Ser825 on the Ago2 peptide by purified Csnk2a1. Substitution of Ser825 to alanine completely abolished phosphorylation, suggesting that Csnk2a1 could phosphorylate Ago2 Ser825 (Figure 5A). Additionally, a global atlas of substrate specificity for the serine/threonine kinome predicted that prior phosphorylation at Ago2 (Ser829) facilitated motif recognition by CK2 at Ser825, implicating hierarchical cooperation between CK1 and CK2.[54] Further *in vitro* phosphorylation using Ago2 peptide pre-phosphorylated at Ser829 demonstrated significantly elevated Ago2 (Ser825) phosphorylation by Csnk2a1 (Figures S5H and S5I), corroborating the notion that CK1-mediated Ago2(Ser829) phosphorylation could prime Ago2(Ser825) for CK2 recognition. Follow-up work using full-length Ago2 in cells is required to validate the role of CK2 and to dissect the stoichiometry and dynamic of the cooperation of CK1 and CK2 in their regulation of Ago2 phosphorylation.

Both Csnk1a1 and Csnk2a1 protein levels were significantly suppressed in K-Ras^{G12D} colonic tissues (Figure 5B). Chromatin accessibility near the transcriptional start sites of Csnk1a1 and Csnk2a1, as well as their RNA levels, also decreased in tissues with K-Ras^{G12D}, suggesting their transcriptional suppression (Figures 5C and 5D). To examine their functional consequences, we inferred CK1/2 kinase activities based on the phospho-levels of their canonical target sites using phospho-proteomics data (Data S3). This kinase enrichment analysis suggested a potential depletion of CK1 and CK2 kinase activities in tissues expressing K-Ras^{G12D}, corroborating their decreased protein level (Figures 5E, 5F, and S5J). Additionally, phosphorylation of Hsp90ab1(Ser226), a canonical target site of Csnk2a1,[55] and the overall CK2 target motif both significantly decreased in the presence of K-Ras^{G12D} *in vivo* (Figures S5K and S5L). Thus, our data suggest that K-Ras^{G12D} suppresses Csnk1a1 and Csnk2a1 protein expression and kinase activity in the colon. However, we were unable to directly quantify Ago2 phosphorylation at Ser825/829/832/835 *in vivo*, as steady-state Ago2 was likely rapidly dephosphorylated by the Ankrd52/Ppp6c complex, rendering these sites largely unphosphorylated without functional KO of the phosphatase.[48]

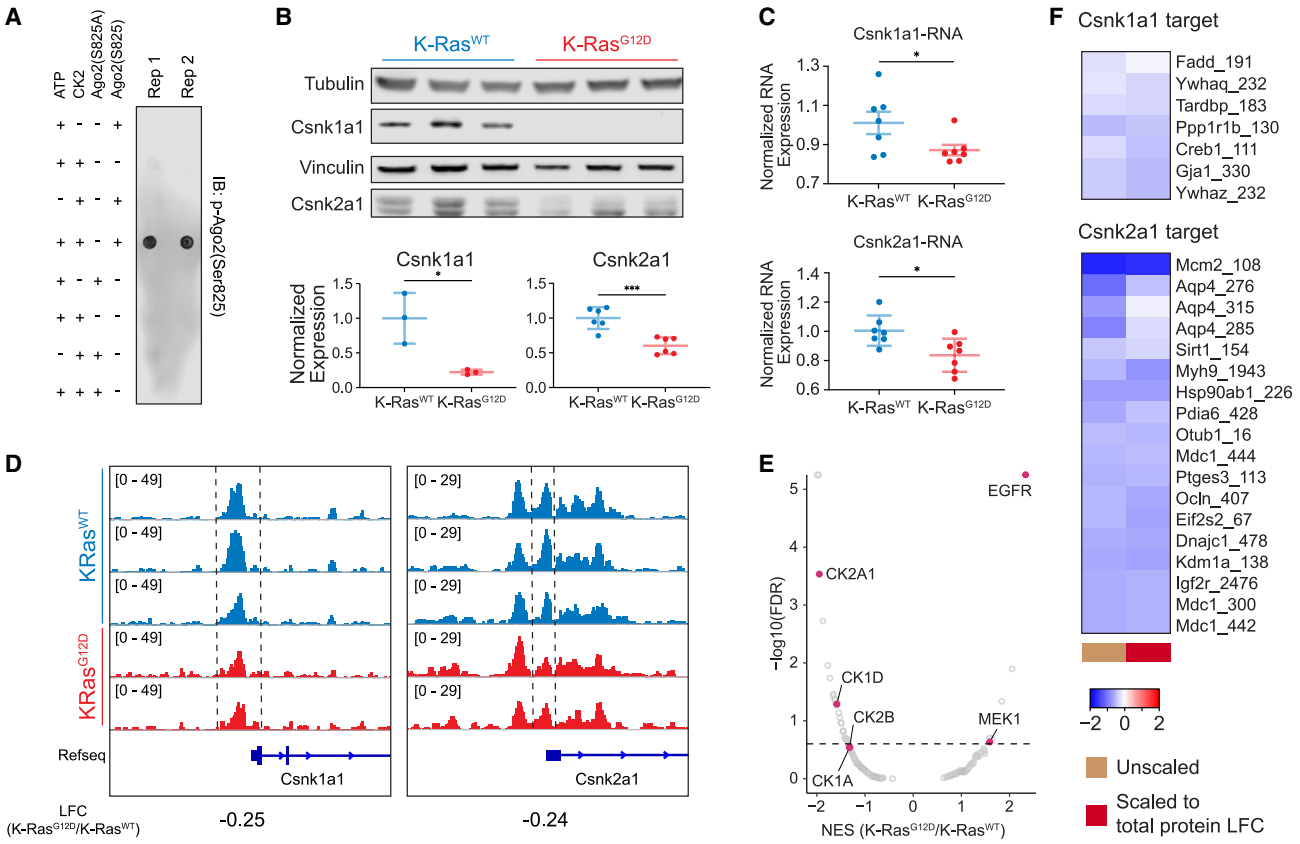

Figure 5. K-Ras^{G12D} suppresses Csnk1a1/Csnk2a1, regulators of Ago2 function

(A) Dot blot showing *in vitro* phosphorylation of the Ago2 (816–838) peptide at Ser825 by purified Csnk2a1. S825A change on the peptide causes complete loss of phosphorylation by Csnk2a1.

(B) Western blotting of endogenous Csnk1a1 and Csnk2a1 in colons ± K-Ras^{G12D}. Error bars represent ±SD. *** $p < 0.001$, * $p < 0.05$ by unpaired t test.

(C) qPCR of Csnk1a1 and Csnk2a1 RNA in colon ± K-Ras^{G12D}. Error bars represent ±SD. * $p < 0.05$ by unpaired t test.

(D) Genome browser view showing the suppression of accessible chromatin near the transcriptional start sites of Csnk1a1 and Csnk2a1 in K-Ras^{G12D} colon.

(E) Volcano plot showing kinase enrichment analysis using K-Ras^{G12D} colonic tumor phospho-proteomic profile. Enrichment is calculated as K-Ras^{G12D} vs. K-Ras^{WT}. Positive NES (net enrichment score) indicates the activation of kinase and vice versa. Canonical Ras pathway kinases EGFR and MEK1 and CK1/2 family members CK1A, CK1D, CK2A1, CK2B are highlighted.

(F) Heatmap showing phosphorylation changes of Csnk1a1 and Csnk2a1 target sites that are detected in the colonic tumor phospho-proteome. Scale bar represents LFC. LFC is calculated as K-Ras^{G12D} vs. K-Ras^{WT}.

See also Figure S5 and Data S3.

Taken together, these data demonstrate that hyperactivated K-Ras signaling in colonic tissues suppresses Csnk1a1/Csnk2a1 kinase activity through transcriptional downregulation, potentially diminishing the steady-state phosphorylation of Ago2 at Ser825/829/832/835, which renders Ago2 non-functional through increased Ago2:mRNA binding that sequesters functional Ago2. This globally suppresses miRNA-mediated gene regulation, causing post-transcriptional upregulation of an extensive network of miRNA target genes upon K-Ras hyperactivation (Figure S5M).

K-Ras/Ago2/miRNA axis in human cancer

Although a general decrease in global miRNA level has been reported in tumors,[56] the pathophysiological impact of global miRNA suppression in cancer remains to be elucidated. CRISPR KO of critical components of the miRNA biogenesis and functional machinery (*Ago2*, *Ankrd52*, *Dicer1*, *Xpo5*, *Tnrc6a*, and *Drosha*) all exerted a negative impact on cancer cell fitness to varying degrees, suggesting anti-tumorigenic effects (Figure 6A). However, this effect was less pronounced in Ras mutant CRC cells, which is consistent with the model that K-Ras mutant cells already have low miRNA activity (Figure S6A). To test this in a genetically controlled system, we generated K-Ras^{WT} and K-Ras^{G12D} primary murine colonic tumor organoids with Ankrd52 KO to fully suppress miRNA function (Figure S6B). While Ankrd52 loss obliterated viability in K-Ras^{WT} organoids, corroborating the anti-tumorigenic effect of global miRNA suppression, K-Ras^{G12D} organoids were resistant to its effect (Figures 6B and S6C). To investigate whether the proposed anti-tumorigenic effect of global miRNA suppression has clinical relevance, we stratified TCGA COAD patients based on their transcriptomic miRNA target signature and observed prolonged survival in

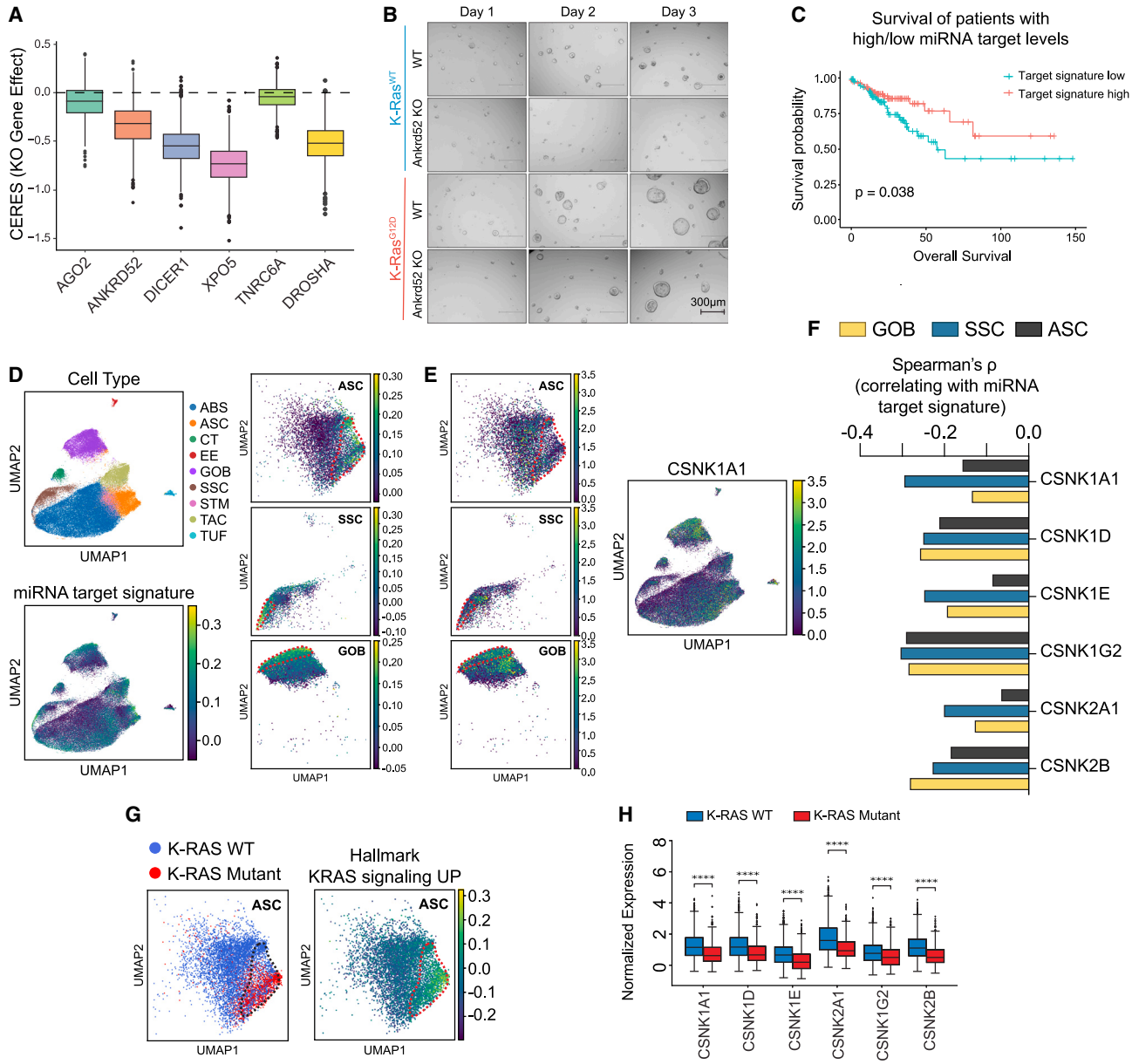

Figure 6. K-Ras/Ago2/miRNA axis in human cancer

(A) DepMap data analysis demonstrating the general negative impact on cancer cell fitness upon CRISPR KO of miRNA machinery key factors.

(B) Bright-field images of WT and Ankrd52 KO mouse colonic tumor organoids ± K-Ras^{G12D} cultured through 72 h showing detrimental effects of global miRNA suppression in K-Ras^{WT} tumor organoids.

(C) Kaplan-Meier plot of CRC patients stratified by their miRNA target signature expression. High target signatures indicate low miRNA activity and vice versa. p value by log-rank test.

(D) UMAPs (Uniform Manifold Approximation and Projection) of cell-type clustering and miRNA target signature in pre-cancerous colonic lesions from patients. Sub-clusters with high miRNA target signature in cell types of interest are highlighted. ABSs, absorptive cells; ASCs,adenoma-specific cells; CTs, crypt top colonocytes; EEs, enteroendocrine cells; GOBs, goblet cells; STMs, stem cells; SSCs, serrated-specific cells; TACs, transit amplifying cells; TUFs, tuft cells.

(E) UMAPs of CSNK1A1 expressions in colorectal patient pre-cancerous lesions. Sub-clusters with high miRNA target signature in cell types of interest are highlighted.

(F) Negative correlations between the expressions of CK1/CK2 family members and miRNA target signature in ASC, SSC, and GOB.

(G) UMAP of K-RAS mutation status and Hallmark KRAS signaling up enrichment in ASC. Sub-clusters with high miRNA target signature in cell types of interest are highlighted, enriched with K-RAS^{Mut} cells.

(H) Boxplot of the expressions of CK1/2 family members in K-RAS^{WT} and K-RAS^{Mut} ASCs showing the suppression of CK1/2 expressions in K-RAS^{Mut} cells. See also Figure S6 and Data S4.

patients with high target signature (a surrogate for suppressed miRNA function) (Figures 6C and S6D; Data S4).

We then set out to understand whether K-Ras signaling was connected to CK1/2 expression and miRNA activity in patients. TCGA (The Cancer Genome Atlas) COAD (colon adenocarcinoma) patients were stratified based on their K-Ras activation status (Data S4). Patients with high/low activation of the K-Ras pathway demonstrated distinct transcriptomic profiles and survival (Figures S6E and S6F). Furthermore, Hallmark pathways enriched in patients with high K-Ras activation resembled those found in K-Ras^{G12D} mouse colonic tumors, highlighting the conservation of transcriptomic signature of hyperactivated K-Ras between mouse and human (Figure S6G). Though *Csnk1a1* and *Csnk2a1* remained unaffected by K-Ras activation, *Csnk1d*, *Csnk1e*, *Csnk1g2*, and *Csnk2b* all experienced decreased expression in patients with hyperactivated K-Ras signaling (Figure S6H). The decrease in Csnk1d levels was recapitulated in mouse colon expressing K-Ras^{G12D} (Figure S6I). Given their homology in the kinase domain, CK1 family kinases have similar substrate specificities.[57] Therefore, it is likely that hyperactivated K-Ras can suppress global miRNA function through inhibition of various CK1/2 kinases. Indeed, a larger proportion of miRNA target genes experienced upregulation in patients with high K-Ras signatures, indicating globally suppressed miRNA activity (Figure S6J).

Given the inter-patient diversity of miRNA target signatures and its correlation with survival, we then inquired whether varying global miRNA activities could also contribute to functional intra-tumoral heterogeneity. Single-cell RNA sequencing (scRNA-seq) of pre-cancerous lesions from colorectal tissues revealed populations with distinct miRNA target signatures in adenoma-specific cells (ASCs), serrated-specific cells (SSCs), and goblet cells (GOBs) (Figure 6D).[58] Activities of individual miRNA families conformed to the general landscape, with populations of high overall miRNA target levels having increased target signatures across all miRNA families, underlying the notion that variances in global miRNA activity, rather than dysregulations of individual miRNAs, were consequential in shaping intra-tumoral heterogeneity (Figures S6K and S6L). While functional enrichment revealed established cell-type-specific signatures, such as enrichment of the Wnt/β-catenin pathway in ASCs and stem cells (STMs) and increased G2M checkpoint/E2F target signatures in the highly proliferative transit amplifying cells (TACs), the clear dichotomy of miRNA target signature, even within the same cell types, contributed to significant functional differences, with cells of high miRNA target levels exhibiting increased protein secretion signature, IRES pathway upregulation, and Rho GTPase activation (Figures S6M and S6N). Dichotomous expression patterns of CK1/2 family kinases were also observed in ASCs, SSCs, and GOBs, each with distinct cell clusters of high/low expression within the same cell type that were of the opposite trend to their miRNA target signatures (Figures 6E and S6O). Overall, expression of all CK1/2 kinases negatively correlated with miRNA target signatures across various cell types, corroborating the model that suppressed CK1/2 expression in tumors impairs global miRNA function to upregulated miRNA targets (Figures 6F and S6P). Integrating patient mutation profiles with scRNA-seq, we focused on samples with various *K-RAS* mutations, which were mostly in the ASCs with heightened K-Ras pathway activation as expected (Figure 6G). K-Ras mutant ASCs had decreased levels of all CK1/2 kinases, further corroborating our proposed model that oncogenic K-Ras suppresses CK1/2 expression/activity and impairs global miRNA function (Figure 6H). Taken together, our data underscored the conservation of the K-Ras/Ago2/miRNA axis in human and its contribution to both inter-patient and intra-tumoral heterogeneity.

DISCUSSION

Oncogenic K-Ras triggers profound transcriptomic and proteomic changes *in vivo*, yet our current understanding of signaling downstream of the activated GTPase offers limited mechanistic insight into how these changes arise. Moreover, understanding the role of K-Ras in miRNA-mediated post-transcriptional regulation has been limited by both the lack of *in vivo* tools and our incomplete understanding of miRNA biology. Using HEAP, we investigated the impact of oncogenic K-Ras on the physiological miRNA target landscape *in vivo*. Through comprehensive integration of chromatic accessibility, transcriptome, miRNA target profile, proteome, and phospho-proteome *in vivo*, we uncovered a surprising global suppression of miRNA function upon K-Ras hyperactivation, paradoxically upregulating hundreds of target genes. The global de-repression of miRNA targets by oncogenic K-Ras was not due to changes in the abundance of miRNAs or the status of functional RISC, but rather through the dysregulation of Ago2 activity itself. Mechanistically, K-Ras^{G12D} induced suppression of Csnk1a1/Csnk2a1 to potentially downregulate Ago2 phosphorylation at Ser825/829/832/835. Hypo-phosphorylated Ago2 exhibits heightened affinity for mRNA target transcripts, resulting in the expanded miRNA target repertoire identified by HEAP. However, this increased binding between Ago2 and mRNA sequestered dynamic and functional Ago2:miRNA complex in a small portion of mRNA, leaving the majority of transcripts un-regulated. This ultimately contributed to the global de-repression of miRNA target genes in colonic tissues with hyperactivated K-Ras signaling.

Consistent with the work we describe in this study, prior circumstantial connections between K-Ras and global suppression of miRNA activity *in vivo* have been reported. We previously demonstrated that the expression of oncogenic K-Ras induced loss of terminally differentiated Paneth cells in the distal small intestine,[31] which was phenocopied by expressing the miRNA suppressive peptide T6B in the intestinal epithelium.[21] Moreover, the suppression of global miRNA activity in T6B-expressing colonic epithelium rendered mice hypersensitive to colonic damage induced by dextran sodium sulfate (DSS), a phenotype that is also observed when K-Ras^{G12D} is expressed.[21] The similarities between these two mouse models suggest that K-Ras could contribute to homeostatic cellular differentiation and the response to pathological stress in the intestinal epithelium by regulating the miRNA network.

Despite their broad targeting, miRNAs are unlikely to always regulate all potential targets. Mechanisms specifying the miRNA:mRNA targeting profile under different conditions remain unclear. Efforts to characterize the physiological function of miRNAs *in vivo* led to the emerging appreciation of the context-specific

nature of miRNA activity. For example, genetic deletion of Dicer, a critical component of miRNA biogenesis machinery, was embryonically lethal due to differentiation defect.[59] Yet, global inhibition of miRNA function in most adult mouse tissues exhibited no clear histologic phenotypes,[21] suggesting that, while crucial during development, miRNA function was dispensable in adult tissues. Given the profiling of physiologic miRNA targets in our study, a particularly interesting outcome is the identification of *miR-194-5p* as an abundant and active miRNA in the colonic tissues, since it has not been extensively characterized in cell culture systems. This underscores the importance of tissue- and context-specific investigation of miRNA functions.

Investigations of miRNA functions regularly follow a linear axis, focusing on changes in just one or a few miRNA target genes. miRNAs are considered "fine tuners" of cellular signaling, as they do not necessarily exert a strong influence on the expression of an individual gene, but rather induce small changes across many targets.[8] Therefore, a system biology approach is necessary to understand miRNA activities holistically. By integrating chromatin landscape, miRNA target profile, transcriptome, and proteome, we unraveled the transcription-independent global de-repression of miRNA targets in tissues expressing oncogenic K-Ras that upregulated hundreds of genes/proteins post-transcriptionally, illuminating another aspect of K-Ras signaling. Previous studies demonstrated that suppression of global miRNA levels was associated with malignancies.[56] Nevertheless, given the scale of genes affected by the global de-repression of miRNA targets, it is limiting to simply pigeonhole the miRNA network as "pro-" or "anti-" tumorigenic. Rather, understanding the ultimate biological effects of broad dysregulation of miRNAs requires systematic dissection of the affected target genes.

In summary, our study presents the *in vivo* characterization of the impact from a single mutation (oncogenic K-Ras) on the physiological miRNA activity landscape. We demonstrate the global suppression of miRNA activity upon hyperactivation of K-Ras that leads to the de-repression of hundreds of miRNA target genes. Our results clarify the underlying mechanism that connects K-Ras to widespread post-transcriptional regulation of gene expression, serving as a foundation to further characterize the influence of oncogenic signaling pathways on the non-coding RNA network.

Limitations of the study

While this study proposes that the global suppression of miRNA activity by oncogenic K-Ras could be attributed to hypo-phosphorylation of Ago2 (Ser825–835), direct quantification of these phosphorylations in tissues was technically challenging. Due to its rapid dephosphorylation by the Ankrd52/Ppp6c complex, Ago2 (Ser825–835) is largely unphosphorylated at steady state. The development of methods for higher sensitivity detection and measurement of phosphorylation in complex environments could further validate the proposed mechanism.

Furthermore, our study demonstrates that oncogenic K-Ras suppresses Csnk1a1/Csnk2a1 and global miRNA activity. Much of the downstream mechanism connecting hyperactive K-Ras signaling to these phenotypes remain unresolved. Several pathways downstream of K-Ras such as MAPK and PI3K/AKT play critical roles in mediating various oncogenic phenotypes and are attractive candidates for further investigation. Studies with a detailed dissection of downstream effectors in vivo are needed to fully elucidate oncogenic K-Ras-mediated global suppression of miRNA activity.

STAR★METHODS

Detailed methods are provided in the online version of this paper and include the following:

- KEY RESOURCES TABLE
- RESOURCE AVAILABILITY
  - Lead contact
  - Materials availability
  - Data and code availability
- EXPERIMENTAL MODEL AND STUDY PARTICIPANT DETAILS
  - Animal models
  - Cell lines and cell culture conditions
  - Organoid lines and culture conditions
- METHOD DETAILS
  - Mouse tissue collection
  - Western blotting
  - Histological characterizations
  - HEAP library preparation
  - RNA-seq library preparation
  - ATAC-seq library preparation
  - miRNA qPCR
  - Halo-Ago2 pull-down qPCR
  - Halo-Ago2 pull-down
  - Size exclusion chromatography
  - RT-qPCR
  - Protein expression and purification
  - *In vitro* peptide phosphorylation
  - Custom antibody development
  - Antibody validation
  - CRISPR knockout of Ankrd52
  - Halo-Ago2 purification followed with MS
  - Organoid viability assay
- QUANTIFICATION AND STATISTICAL ANALYSIS
  - Histological measurements
  - HEAP processing
  - HEAP analysis
  - RNA-seq processing and analysis
  - PAGE Z-score calculation
  - MS-based proteomic and phospho-proteomic analysis
  - ATAC-seq processing and analysis
  - Gene set enrichment analysis
  - Kinase enrichment analysis
  - DepMap analysis
  - TCGA analysis
  - scRNA-seq analysis

SUPPLEMENTAL INFORMATION

Supplemental information can be found online at https://doi.org/10.1016/j.molcel.2023.06.008.

ACKNOWLEDGMENTS

Thank you to the members of the Haigis lab, particularly Shikha Sheth, Olesja Popow, Christian Johnson, and Yi-Jang Lin for their feedback, and to Anna M. Schmoker for her guidance on mass spectrometry. We are also grateful to the imaging support from Neurobiology Imaging Facility of HMS (NINDS P30 Core Center Grant #NS072030), high-performance computing from HMS Research Computing, and bioinformatics consultation from Harvard Chan Bioinformatics Core. Some figures were created with BioRender.com. This work was supported by grants from the National Institutes of Health (R01CA178017 and R01CA232372 to K.M.H., R01CA149707 and R01CA245507 to A.V., and R01DK103831 and P50CA236733 to K.S.L.) and an award from the Cancer Research UK Grand Challenge and the Mark Foundation to the SPECIFICANCER team. K.M.H. is also supported by the Dana-Farber Cancer Institute Hale Center for Pancreatic Cancer Research and the Project P fund. T.S.B. is supported by a Ruth L. Kirschstein National Research Service Award (5F32CA247198-02). B.S. was supported by the Landry Cancer Biology Research Fellowship, the Albert J. Ryan Fellowship, and the Jean Strouse Sharf and Lisa Sharf Green Cancer Research Fund in memory of Evelyn P. Strouse.

AUTHOR CONTRIBUTIONS

Conceptualization, B.S., A.V., and K.M.H.; methodology, B.S., T.S.B., X.L., G.L.R., M.J.E., K.S.L, A.V., and K.M.H.; investigation, B.S., T.S.B., Z.C., and G.L.R.; formal analysis, B.S., Z.C., X.L., and W.M.G.; resources, B.S., T.S.B., X.L., and G.L.R.; data curation, B.S.; writing – original draft, B.S. and K.M.H.; writing – review & editing, B.S., T.S.B., Z.C., X.L., G.L.R., M.J.E., K.S.L., A.V., and K.M.H.; supervision, M.J.E., K.S.L., A.V., and K.M.H.; funding acquisition, A.V. and K.M.H.

DECLARATION OF INTERESTS

K.M.H. is married to a member of *Molecular Cell*'s Advisory Board.

Received: November 2, 2022
Revised: May 5, 2023
Accepted: June 5, 2023
Published: July 3, 2023

REFERENCES

1. Haigis, K.M. (2017). KRAS alleles: the devil is in the detail. Trends Cancer *3*, 686–697. https://doi.org/10.1016/j.trecan.2017.08.006.
2. Hingorani, S.R., Petricoin, E.F., Maitra, A., Rajapakse, V., King, C., Jacobetz, M.A., Ross, S., Conrads, T.P., Veenstra, T.D., Hitt, B.A., et al. (2003). Preinvasive and invasive ductal pancreatic cancer and its early detection in the mouse. Cancer Cell *4*, 437–450. https://doi.org/10.1016/s1535-6108(03)00309-x.
3. Tuveson, D.A., Shaw, A.T., Willis, N.A., Silver, D.P., Jackson, E.L., Chang, S., Mercer, K.L., Grochow, R., Hock, H., Crowley, D., et al. (2004). Endogenous oncogenic K-rasG12D stimulates proliferation and widespread neoplastic and developmental defects. Cancer Cell *5*, 375–387. https://doi.org/10.1016/S1535-6108(04)00085-6.
4. Jackson, E.L., Willis, N., Mercer, K., Bronson, R.T., Crowley, D., Montoya, R., Jacks, T., and Tuveson, D.A. (2001). Analysis of lung tumor initiation and progression using conditional expression of oncogenic K-ras. Genes Dev. *15*, 3243–3248. https://doi.org/10.1101/gad.943001.
5. Johnson, L., Mercer, K., Greenbaum, D., Bronson, R.T., Crowley, D., Tuveson, D.A., and Jacks, T. (2001). Somatic activation of the K-ras oncogene causes early onset lung cancer in mice. Nature *410*, 1111–1116. https://doi.org/10.1038/35074129.
6. Haigis, K.M., Kendall, K.R., Wang, Y., Cheung, A., Haigis, M.C., Glickman, J.N., Niwa-Kawakita, M., Sweet-Cordero, A., Sebolt-Leopold, J., Shannon, K.M., et al. (2008). Differential effects of oncogenic K-Ras and N-Ras on proliferation, differentiation and tumor progression in the colon. Nat. Genet. *40*, 600–608. https://doi.org/10.1038/ng.115.
7. Braun, B.S., Tuveson, D.A., Kong, N., Le, D.T., Kogan, S.C., Rozmus, J., Le Beau, M.M.L., Jacks, T.E., and Shannon, K.M. (2004). Somatic activation of oncogenic Kras in hematopoietic cells initiates a rapidly fatal myeloproliferative disorder. Proc. Natl. Acad. Sci. USA *101*, 597–602. https://doi.org/10.1073/pnas.0307203101.
8. Bartel, D.P. (2018). Metazoan microRNAs. Cell *173*, 20–51. https://doi.org/10.1016/j.cell.2018.03.006.
9. Müller, M., Fazi, F., and Ciaudo, C. (2019). Argonaute proteins: from structure to function in development and pathological cell fate determination. Front. Cell Dev. Biol. *7*, 360. https://doi.org/10.3389/fcell.2019.00360.
10. Ha, M., and Kim, V.N. (2014). Regulation of microRNA biogenesis. Nat. Rev. Mol. Cell Biol. *15*, 509–524. https://doi.org/10.1038/nrm3838.
11. Duchaine, T.F., and Fabian, M.R. (2019). Mechanistic insights into microRNA-mediated gene silencing. Cold Spring Harb. Perspect. Biol. *11*, a032771. https://doi.org/10.1101/cshperspect.a032771.
12. Braun, J.E., Huntzinger, E., Fauser, M., and Izaurralde, E. (2011). GW182 proteins directly recruit cytoplasmic deadenylase complexes to miRNA targets. Mol. Cell *44*, 120–133. https://doi.org/10.1016/j.molcel.2011.09.007.
13. Nishihara, T., Zekri, L., Braun, J.E., and Izaurralde, E. (2013). miRISC recruits decapping factors to miRNA targets to enhance their degradation. Nucleic Acids Res. *41*, 8692–8705. https://doi.org/10.1093/nar/gkt619.
14. Agarwal, V., Bell, G.W., Nam, J.W., and Bartel, D.P. (2015). Predicting effective microRNA target sites in mammalian mRNAs. eLife *4*, e05005. https://doi.org/10.7554/eLife.05005.
15. Reinhart, B.J., Slack, F.J., Basson, M., Pasquinelli, A.E., Bettinger, J.C., Rougvie, A.E., Horvitz, H.R., and Ruvkun, G. (2000). The 21-nucleotide let-7 RNA regulates developmental timing in Caenorhabditis elegans. Nature *403*, 901–906. https://doi.org/10.1038/35002607.
16. Johnson, S.M., Grosshans, H., Shingara, J., Byrom, M., Jarvis, R., Cheng, A., Labourier, E., Reinert, K.L., Brown, D., and Slack, F.J. (2005). RAS Is Regulated by the let-7 microRNA Family. Cell *120*, 635–647. https://doi.org/10.1016/j.cell.2005.01.014.
17. Valencia, K., Erice, O., Kostyrko, K., Hausmann, S., Guruceaga, E., Tathireddy, A., Flores, N.M., Sayles, L.C., Lee, A.G., Fragoso, R., et al. (2020). The Mir181ab1 cluster promotes KRAS-driven oncogenesis and progression in lung and pancreas. J. Clin. Invest. *130*, 1879–1895. https://doi.org/10.1172/JCI129012.
18. Krek, A., Grün, D., Poy, M.N., Wolf, R., Rosenberg, L., Epstein, E.J., MacMenamin, P., Piedade da, I., Gunsalus, K.C., Stoffel, M., et al. (2005). Combinatorial microRNA target predictions. Nat. Genet. *37*, 495–500. https://doi.org/10.1038/ng1536.
19. Enright, A.J., John, B., Gaul, U., Tuschl, T., Sander, C., and Marks, D.S. (2003). MicroRNA targets in Drosophila. Genome Biol. *5*, R1. https://doi.org/10.1186/gb-2003-5-1-r1.
20. La Rocca, G., Olejniczak, S.H., González, A.J., Briskin, D., Vidigal, J.A., Spraggon, L., DeMatteo, R.G., Radler, M.R., Lindsten, T., Ventura, A., et al. (2015). In vivo, Argonaute-bound microRNAs exist predominantly in a reservoir of low molecular weight complexes not associated with mRNA. Proc. Natl. Acad. Sci. USA *112*, 767–772. https://doi.org/10.1073/pnas.1424217112.
21. La Rocca, G., King, B., Shui, B., Li, X., Zhang, M., Akat, K.M., Ogrodowski, P., Mastroleo, C., Chen, K., Cavalieri, V., et al. (2021). Inducible and reversible inhibition of miRNA-mediated gene repression in vivo. eLife *10*, e70948. https://doi.org/10.7554/eLife.70948.
22. Chi, S.W., Zang, J.B., Mele, A., and Darnell, R.B. (2009). Argonaute HITS-CLIP decodes microRNA-mRNA interaction maps. Nature *460*, 479–486. https://doi.org/10.1038/nature08170.
23. König, J., Zarnack, K., Rot, G., Curk, T., Kayikci, M., Zupan, B., Turner, D.J., Luscombe, N.M., and Ule, J. (2010). iCLIP reveals the function of hnRNP particles in splicing at individual nucleotide resolution. Nat. Struct. Mol. Biol. *17*, 909–915. https://doi.org/10.1038/nsmb.1838.

24. Helwak, A., Kudla, G., Dudnakova, T., and Tollervey, D. (2013). Mapping the human miRNA interactome by CLASH reveals frequent noncanonical binding. Cell *153*, 654–665. https://doi.org/10.1016/j.cell.2013.03.043.

25. Van Nostrand, E.L.V., Pratt, G.A., Shishkin, A.A., Gelboin-Burkhart, C., Fang, M.Y., Sundararaman, B., Blue, S.M., Nguyen, T.B., Surka, C., Elkins, K., et al. (2016). Robust transcriptome-wide discovery of RNA-binding protein binding sites with enhanced CLIP (eCLIP). Nat. Methods *13*, 508–514. https://doi.org/10.1038/nmeth.3810.

26. Li, X., Pritykin, Y., Concepcion, C.P., Lu, Y., La Rocca, G., Zhang, M., King, B., Cook, P.J., Au, Y.W., Popow, O., et al. (2020). High-resolution in vivo identification of miRNA targets by halo-enhanced Ago2 pull-down. Mol. Cell *79*, 167–179.e11. https://doi.org/10.1016/j.molcel.2020.05.009.

27. Saam, J.R., and Gordon, J.I. (1999). Inducible gene knockouts in the small intestinal and colonic epithelium. J. Biol. Chem. *274*, 38071–38082. https://doi.org/10.1074/jbc.274.53.38071.

28. el Marjou, F.E., Janssen, K.P., Chang, B.H., Li, M., Hindie, V., Chan, L., Louvard, D., Chambon, P., Metzger, D., and Robine, S. (2004). Tissue-specific and inducible Cre-mediated recombination in the gut epithelium. Genesis *39*, 186–193. https://doi.org/10.1002/gene.20042.

29. Kuraguchi, M., Wang, X.P., Bronson, R.T., Rothenberg, R., Ohene-Baah, N.Y., Lund, J.J., Kucherlapati, M., Maas, R.L., and Kucherlapati, R. (2006). Adenomatous polyposis coli (APC) is required for normal development of skin and Thymus. PLoS Genet. *2*, e146. https://doi.org/10.1371/journal.pgen.0020146.

30. Jones, R.P., Sutton, P.A., Evans, J.P., Clifford, R., McAvoy, A., Lewis, J., Rousseau, A., Mountford, R., McWhirter, D., and Malik, H.Z. (2017). Specific mutations in KRAS codon 12 are associated with worse overall survival in patients with advanced and recurrent colorectal cancer. Br. J. Cancer *116*, 923–929. https://doi.org/10.1038/bjc.2017.37.

31. Poulin, E.J., Bera, A.K., Lu, J., Lin, Y.J., Strasser, S.D., Paulo, J.A., Huang, T.Q., Morales, C., Yan, W., Cook, J., et al. (2019). Tissue-specific oncogenic activity of KRASA146T. Cancer Discov. *9*, 738–755. https://doi.org/10.1158/2159-8290.CD-18-1220.

32. Kobayashi, M., Benakis, C., Anderson, C., Moore, M.J., Poon, C., Uekawa, K., Dyke, J.P., Fak, J.J., Mele, A., Park, C.Y., et al. (2019). AGO CLIP reveals an activated network for acute regulation of brain glutamate homeostasis in ischemic stroke. Cell Rep. *28*, 979–991.e6. https://doi.org/10.1016/j.celrep.2019.06.075.

33. Kim, S.Y., and Volsky, D.J. (2005). PAGE: parametric analysis of gene set enrichment. BMC Bioinformatics *6*, 144. https://doi.org/10.1186/1471-2105-6-144.

34. Brubaker, D.K., Paulo, J.A., Sheth, S., Poulin, E.J., Popow, O., Joughin, B.A., Strasser, S.D., Starchenko, A., Gygi, S.P., Lauffenburger, D.A., et al. (2019). Proteogenomic network analysis of context-specific KRAS signaling in mouse-to-human cross-species translation. Cell Syst. *9*, 258–270.e6. https://doi.org/10.1016/j.cels.2019.07.006.

35. de la Torre-Ubieta, L., Stein, J.L., Won, H., Opland, C.K., Liang, D., Lu, D., and Geschwind, D.H. (2018). The dynamic landscape of open chromatin during human cortical neurogenesis. Cell *172*, 289–304.e18. https://doi.org/10.1016/j.cell.2017.12.014.

36. González, A.J., Setty, M., and Leslie, C.S. (2015). Early enhancer establishment and regulatory locus complexity shape transcriptional programs in hematopoietic differentiation. Nat. Genet. *47*, 1249–1259. https://doi.org/10.1038/ng.3402.

37. Johnson, C.D., Esquela-Kerscher, A., Stefani, G., Byrom, M., Kelnar, K., Ovcharenko, D., Wilson, M., Wang, X., Shelton, J., Shingara, J., et al. (2007). The let-7 microRNA Represses Cell Proliferation Pathways in Human Cells. Cancer Res. *67*, 7713–7722. https://doi.org/10.1158/0008-5472.CAN-07-1083.

38. Bargaje, R., Gupta, S., Sarkeshik, A., Park, R., Xu, T., Sarkar, M., Halimani, M., Roy, S.S., Yates, J., and Pillai, B. (2012). Identification of novel targets for miR-29a using miRNA proteomics. PLoS One *7*, e43243. https://doi.org/10.1371/journal.pone.0043243.

39. Kopp, F., Wagner, E., and Roidl, A. (2014). The proto-oncogene KRAS is targeted by miR-200c. Oncotarget *5*, 185–195. https://doi.org/10.18632/oncotarget.1427.

40. Ventura, A., Young, A.G., Winslow, M.M., Lintault, L., Meissner, A., Erkeland, S.J., Newman, J., Bronson, R.T., Crowley, D., Stone, J.R., et al. (2008). Targeted deletion reveals essential and overlapping functions of the miR-17∼92 family of miRNA clusters. Cell *132*, 875–886. https://doi.org/10.1016/j.cell.2008.02.019.

41. Shi, L., Middleton, J., Jeon, Y.J., Magee, P., Veneziano, D., Laganà, A., Leong, H.S., Sahoo, S., Fassan, M., Booton, R., et al. (2018). KRAS induces lung tumorigenesis through microRNAs modulation. Cell Death Dis. *9*, 219. https://doi.org/10.1038/s41419-017-0243-9.

42. Iliopoulos, D., Rotem, A., and Struhl, K. (2011). Inhibition of miR-193a expression by max and RXRα activates K-Ras and PLAU to mediate distinct aspects of cellular transformation. Cancer Res. *71*, 5144–5153. https://doi.org/10.1158/0008-5472.CAN-11-0425.

43. Shankar, S., Pitchiaya, S., Malik, R., Kothari, V., Hosono, Y., Yocum, A.K., Gundlapalli, H., White, Y., Firestone, A., Cao, X., et al. (2016). KRAS engages AGO2 to enhance cellular transformation. Cell Rep. *14*, 1448–1461. https://doi.org/10.1016/j.celrep.2016.01.034.

44. Zeng, Y., Sankala, H., Zhang, X., and Graves, P.R. (2008). Phosphorylation of Argonaute 2 at serine-387 facilitates its localization to processing bodies. Biochem. J. *413*, 429–436. https://doi.org/10.1042/BJ20080599.

45. Horman, S.R., Janas, M.M., Litterst, C., Wang, B., MacRae, I.J., Sever, M.J., Morrissey, D.V., Graves, P., Luo, B., Umesalma, S., et al. (2013). Akt-mediated phosphorylation of argonaute 2 downregulates cleavage and upregulates translational repression of microRNA targets. Mol. Cell *50*, 356–367. https://doi.org/10.1016/j.molcel.2013.03.015.

46. Rüdel, S., Wang, Y., Lenobel, R., Körner, R., Hsiao, H.H., Urlaub, H., Patel, D., and Meister, G. (2011). Phosphorylation of human Argonaute proteins affects small RNA binding. Nucleic Acids Res. *39*, 2330–2343. https://doi.org/10.1093/nar/gkq1032.

47. Shen, J., Xia, W., Khotskaya, Y.B., Huo, L., Nakanishi, K., Lim, S.O., Du, Y., Wang, Y., Chang, W.C., Chen, C.H., et al. (2013). EGFR modulates microRNA maturation in response to hypoxia through phosphorylation of AGO2. Nature *497*, 383–387. https://doi.org/10.1038/nature12080.

48. Golden, R.J., Chen, B., Li, T., Braun, J., Manjunath, H., Chen, X., Wu, J., Schmid, V., Chang, T.C., Kopp, F., et al. (2017). An Argonaute phosphorylation cycle promotes microRNA-mediated silencing. Nature *542*, 197–202. https://doi.org/10.1038/nature21025.

49. Quévillon Huberdeau, M.Q., Zeitler, D.M., Hauptmann, J., Bruckmann, A., Fressigné, L., Danner, J., Piquet, S., Strieder, N., Engelmann, J.C., Jannot, G., et al. (2017). Phosphorylation of Argonaute proteins affects mRNA binding and is essential for microRNA-guided gene silencing in vivo. EMBO J. *36*, 2088–2106. https://doi.org/10.15252/embj.201696386.

50. Bibel, B., Elkayam, E., Silletti, S., Komives, E.A., and Joshua-Tor, L. (2022). Target binding triggers hierarchical phosphorylation of human Argonaute-2 to promote target release. eLife *11*, e76908. https://doi.org/10.7554/eLife.76908.

51. Obenauer, J.C., Cantley, L.C., and Yaffe, M.B. (2003). Scansite 2.0: proteome-wide prediction of cell signaling interactions using short sequence motifs. Nucleic Acids Res. *31*, 3635–3641. https://doi.org/10.1093/nar/gkg584.

52. Horn, H., Schoof, E.M., Kim, J., Robin, X., Miller, M.L., Diella, F., Palma, A., Cesareni, G., Jensen, L.J., and Linding, R. (2014). KinomeXplorer: an integrated platform for kinome biology studies. Nat. Methods *11*, 603–604. https://doi.org/10.1038/nmeth.2968.

53. Borgo, C., D'Amore, C., Sarno, S., Salvi, M., and Ruzzene, M. (2021). Protein kinase CK2: a potential therapeutic target for diverse human diseases. Signal Transduct. Target. Ther. *6*, 183. https://doi.org/10.1038/s41392-021-00567-7.

54. Johnson, J.L., Yaron, T.M., Huntsman, E.M., Kerelsky, A., Song, J., Regev, A., Lin, T.-Y., Liberatore, K., Cizin, D.M., Cohen, B.M., et al. (2022). A

global atlas of substrate specificities for the human serine/threonine kinome. Preprint at bioRxiv. https://doi.org/10.1101/2022.05.22.492882.

55. Lees-Miller, S.P., and Anderson, C.W. (1989). Two human 90-kDa heat shock proteins are phosphorylated in vivo at conserved serines that are phosphorylated in vitro by casein kinase II. J. Biol. Chem. *264*, 2431–2437.

56. Lu, J., Getz, G., Miska, E.A., Alvarez-Saavedra, E., Lamb, J., Peck, D., Sweet-Cordero, A., Ebert, B.L., Mak, R.H., Ferrando, A.A., et al. (2005). MicroRNA expression profiles classify human cancers. Nature *435*, 834–838. https://doi.org/10.1038/nature03702.

57. Jiang, J. (2017). CK1 in developmental signaling: hedgehog and Wnt. Curr. Top. Dev. Biol. *123*, 303–329. https://doi.org/10.1016/bs.ctdb.2016.09.002.

58. Chen, B., Scurrah, C.R., McKinley, E.T., Simmons, A.J., Ramirez-Solano, M.A., Zhu, X., Markham, N.O., Heiser, C.N., Vega, P.N., Rolong, A., et al. (2021). Differential pre-malignant programs and microenvironment chart distinct paths to malignancy in human colorectal polyps. Cell *184*, 6262–6280.e26. https://doi.org/10.1016/j.cell.2021.11.031.

59. Bernstein, E., Kim, S.Y., Carmell, M.A., Murchison, E.P., Alcorn, H., Li, M.Z., Mills, A.A., Elledge, S.J., Anderson, K.V., and Hannon, G.J. (2003). Dicer is essential for mouse development. Nat. Genet. *35*, 215–217. https://doi.org/10.1038/ng1253.

60. Martin, M. (2011). Cutadapt removes adapter sequences from high-throughput sequencing reads. EMBnet J. *17*, 10–12. https://doi.org/10.14806/ej.17.1.200.

61. Dobin, A., Davis, C.A., Schlesinger, F., Drenkow, J., Zaleski, C., Jha, S., Batut, P., Chaisson, M., and Gingeras, T.R. (2013). STAR: ultrafast universal RNA-seq aligner. Bioinformatics *29*, 15–21. https://doi.org/10.1093/bioinformatics/bts635.

62. Danecek, P., Bonfield, J.K., Liddle, J., Marshall, J., Ohan, V., Pollard, M.O., Whitwham, A., Keane, T., McCarthy, S.A., Davies, R.M., et al. (2021). Twelve years of SAMtools and BCFtools. GigaScience *10*, giab008. https://doi.org/10.1093/gigascience/giab008.

63. Pantano, L., Estivill, X., and Martí, E. (2011). A non-biased framework for the annotation and classification of the non-miRNA small RNA transcriptome. Bioinformatics *27*, 3202–3203. https://doi.org/10.1093/bioinformatics/btr527.

64. Lawrence, M., Huber, W., Pagès, H., Aboyoun, P., Carlson, M., Gentleman, R., Morgan, M.T., and Carey, V.J. (2013). Software for computing and annotating genomic ranges. PLoS Comput. Biol. *9*, e1003118. https://doi.org/10.1371/journal.pcbi.1003118.

65. Liao, Y., Smyth, G.K., and Shi, W. (2019). The R package Rsubread is easier, faster, cheaper and better for alignment and quantification of RNA sequencing reads. Nucleic Acids Res. *47*, e47. https://doi.org/10.1093/nar/gkz114.

66. Love, M.I., Huber, W., and Anders, S. (2014). Moderated estimation of fold change and dispersion for RNA-seq data with DESeq2. Genome Biol. *15*, 550. https://doi.org/10.1186/s13059-014-0550-8.

67. Heinz, S., Benner, C., Spann, N., Bertolino, E., Lin, Y.C., Laslo, P., Cheng, J.X., Murre, C., Singh, H., and Glass, C.K. (2010). Simple combinations of lineage-determining transcription factors prime cis-regulatory elements required for macrophage and B cell identities. Mol. Cell *38*, 576–589. https://doi.org/10.1016/j.molcel.2010.05.004.

68. Yu, G., Wang, L.G., Han, Y., and He, Q.Y. (2012). clusterProfiler: an R package for comparing biological themes among gene clusters. Omics J. Integr. Biol. *16*, 284–287. https://doi.org/10.1089/omi.2011.0118.

69. Patro, R., Duggal, G., Love, M.I., Irizarry, R.A., and Kingsford, C. (2017). Salmon provides fast and bias-aware quantification of transcript expression. Nat. Methods *14*, 417–419. https://doi.org/10.1038/nmeth.4197.

70. Wang, Q., Li, M., Wu, T., Zhan, L., Li, L., Chen, M., Xie, W., Xie, Z., Hu, E., Xu, S., et al. (2022). Exploring epigenomic datasets by ChIPseeker. Curr. Protoc. *2*, e585. https://doi.org/10.1002/cpz1.585.

71. Subramanian, A., Tamayo, P., Mootha, V.K., Mukherjee, S., Ebert, B.L., Gillette, M.A., Paulovich, A., Pomeroy, S.L., Golub, T.R., Lander, E.S., et al. (2005). Gene set enrichment analysis: a knowledge-based approach for interpreting genome-wide expression profiles. Proc. Natl. Acad. Sci. USA *102*, 15545–15550. https://doi.org/10.1073/pnas.0506580102.

72. Hänzelmann, S., Castelo, R., and Guinney, J. (2013). GSVA: gene set variation analysis for microarray and RNA-seq data. BMC Bioinformatics *14*, 7. https://doi.org/10.1186/1471-2105-14-7.

73. Virtanen, P., Gommers, R., Oliphant, T.E., Haberland, M., Reddy, T., Cournapeau, D., Burovski, E., Peterson, P., Weckesser, W., Bright, J., et al. (2020). SciPy 1.0: fundamental algorithms for scientific computing in Python. Nat. Methods *17*, 261–272. https://doi.org/10.1038/s41592-019-0686-2.

74. Ritchie, M.E., Phipson, B., Wu, D., Hu, Y., Law, C.W., Shi, W., and Smyth, G.K. (2015). limma powers differential expression analyses for RNA-sequencing and microarray studies. Nucleic Acids Res. *43*, e47. https://doi.org/10.1093/nar/gkv007.

75. Waters, A.M., Ozkan-Dagliyan, I., Vaseva, A.V., Fer, N., Strathern, L.A., Hobbs, G.A., Tessier-Cloutier, B., Gillette, W.K., Bagni, R., Whiteley, G.R., et al. (2017). Evaluation of the selectivity and sensitivity of isoform- and mutation-specific RAS antibodies. Sci. Signal. *10*. https://doi.org/10.1126/scisignal.aao3332.

76. Shankar, S., Tien, J.C.-Y., Siebenaler, R.F., Chugh, S., Dommeti, V.L., Zelenka-Wang, S., Wang, X.M., Apel, I.J., Waninger, J., Eyunni, S., et al. (2020). An essential role for Argonaute 2 in EGFR-KRAS signaling in pancreatic cancer development. Nat. Commun. *11*, 2817. https://doi.org/10.1038/s41467-020-16309-2.

77. Sharova, L.V., Sharov, A.A., Nedorezov, T., Piao, Y., Shaik, N., and Ko, M.S.H. (2009). Database for mRNA half-life of 19 977 genes obtained by DNA microarray analysis of pluripotent and differentiating mouse embryonic stem cells. DNA Res. *16*, 45–58. https://doi.org/10.1093/dnares/dsn030.

78. Amemiya, H.M., Kundaje, A., and Boyle, A.P. (2019). The ENCODE blacklist: identification of problematic regions of the genome. Sci. Rep. *9*, 9354. https://doi.org/10.1038/s41598-019-45839-z.

79. Strasser, S.D., Ghazi, P.C., Starchenko, A., Boukhali, M., Edwards, A., Suarez-Lopez, L., Lyons, J., Changelian, P.S., Monahan, J.B., Jacobsen, J., et al. (2019). Substrate-based kinase activity inference identifies MK2 as driver of colitis. Integr. Biol. (Camb) *11*, 301–314. https://doi.org/10.1093/intbio/zyz025.

80. Hoadley, K.A., Yau, C., Hinoue, T., Wolf, D.M., Lazar, A.J., Drill, E., Shen, R., Taylor, A.M., Cherniack, A.D., Thorsson, V., et al. (2018). Cell-of-origin patterns dominate the molecular classification of 10,000 tumors from 33 types of cancer. Cell *173*, 291–304.e6. https://doi.org/10.1016/j.cell.2018.03.022.

81. Heiser, C.N., Wang, V.M., Chen, B., Hughey, J.J., and Lau, K.S. (2021). Automated quality control and cell identification of droplet-based single-cell data using dropkick. Genome Res. *31*, 1742–1752. https://doi.org/10.1101/gr.271908.120.

82. Van de Sande, B., Flerin, C., Davie, K., De Waegeneer, M., Hulselmans, G., Aibar, S., Seurinck, R., Saelens, W., Cannoodt, R., Rouchon, Q., et al. (2020). A scalable SCENIC workflow for single-cell gene regulatory network analysis. Nat. Protoc. *15*, 2247–2276. https://doi.org/10.1038/s41596-020-0336-2.

83. Aibar, S., González-Blas, C.B., Moerman, T., Huynh-Thu, V.A., Imrichova, H., Hulselmans, G., Rambow, F., Marine, J.C., Geurts, P., Aerts, J., et al. (2017). SCENIC: single-cell regulatory network inference and clustering. Nat. Methods *14*, 1083–1086. https://doi.org/10.1038/nmeth.4463.

STAR★METHODS

KEY RESOURCES TABLE

REAGENT or RESOURCE	SOURCE	IDENTIFIER
Antibodies		
Ras	Millipore	05-516; RRID: AB_11211664
Ras^{G12D}	Cell Signaling Technology	14429; RRID: AB_2728748
K-Ras	Millipore	OP-24; RRID: AB_2134115
Gapdh	Cell Signaling Technology	5174; RRID: AB_10622025
Erk	Cell Signaling Technology	4696; RRID: AB_390780
p-Erk(Thr202/Tyr204)	Cell Signaling Technology	4377; RRID: AB_331775
Vinculin	Cell Signaling Technology	13901; RRID: AB_2728768
Mek	Cell Signaling Technology	4694; RRID: AB_10695868
p-Mek(Ser217/221)	Cell Signaling Technology	9121; RRID: AB_331648
Ago2	Cell Signaling Technology	2897; RRID: AB_2096291
HaloTag	Promega	G9211; RRID: AB_2688011
Tubulin	Calbiochem	CP06; RRID: AB_2617116
Tnrc6a	Bethyl Laboratories	A302-329A-M; RRID: AB_2780472
Csnk1a1	Santa-Cruz Biotechnology	sc-74582; RRID: AB_2084662
Csnk2a1	Cell Signaling Technology	2656; RRID: AB_2236816
Ppp6c	Abcam	ab131335; RRID: AB_11155732
Ankrd52	LSBio	LS-C483018; RRID: AB_2940851
Hsp90ab1	Cell Signaling Technology	5087; RRID: AB_10548761
p-Hsp90ab1(Ser226)	LSBio	LS-C359019; RRID: AB_2940852
CK2 phospho-motif	Cell Signaling Technology	8738; RRID: AB_2797653
Csnk1d	Santa Cruz Biotechnology	sc-514942; RRID: AB_2940853
Alexa Fluor Plus 800 Goat anti-Rabbit IgG	Invitrogen	A32735; RRID: AB_2633284
Alexa Fluor 680 Goat anti-Mouse IgG	Invitrogen	A21058; RRID: AB_2535724
p-Ago2(Ser825)	This paper	NA
Ki67	Cell Signaling Technology	12202; RRID: AB_2620142
p-Erk(Thr202/Tyr204)	Cell Signaling Technology	9101; RRID: AB_331646
Lysozyme	ThermoFisher	RB-372-A1; RRID: AB_138387
E-Cadherin	BD Biosciences	610181; RRID: AB_397580
β-catenin	Cell Signaling Technology	9562; RRID: AB_331149
Envision+ HRP conjugated anti-rabbit polymers	Agilent	K400311-2; RRID: AB_2827819
Alexa Fluor 647 Goat anti-Rabbit IgG	Invitrogen	A21244; RRID: AB_2535812
Alexa Fluor 488 Goat anti-Rabbit IgG	Invitrogen	A11034; RRID: AB_2576217
Alexa Fluor 594 Goat anti-Mouse IgG2a	Invitrogen	A21135; RRID: AB_2535774
Chemicals, peptides, and recombinant proteins		
4-hydroxytamixofen (4-OHT)	Sigma-aldrich	T176
Advanced DMEM/F12	GIBCO	12634028
B-27	GIBCO	17504044
N-2	GIBCO	17502048
Glutamax	GIBCO	35050061
HEPES	GIBCO	15630080
Nicotinamide	Sigma-aldrich	N0636
N-Acetylcysteine	Sigma-aldrich	A0737

(*Continued on next page*)

Continued

REAGENT or RESOURCE	SOURCE	IDENTIFIER
[Leu15]-Gastrin I Human	Sigma-aldrich	G9145
A83-01	Sigma-aldrich	SML0788
SB-202190	Sigma-aldrich	S7067
Recombinant human EGF	ThermoFisher	PHG0311
Prostaglandin E2	Sigma-aldrich	P0409
Primocin	InvivGgen	ANT-PM-1
Noggin	PeproTech	25038250UG
Bioplex lysis buffer	Bio-rad	171304011
cOmplete™ EDTA-free protease inhibitor cocktail	Millipore-Sigma	11873580001
Histo-Clear	National Diagnostics	HS2001GLL
pH6.1 target retrieval solutions	Dako	S1699
pH9 target retrieval solutions	Dako	S2367
DAPI	BD Biosciences	564907
HaloLink resin	Promega	G1914
Protease Inhibitor	Promega	G6521
RNasin Ribonuclease Inhibitor	Promega	N2515
HaloTEV protease	Promega	G6602
Phosphatase inhibitor cocktail 2	Sigma-aldrich	P5726
Phosphatase inhibitor cocktail 3	Sigma-aldrich	P0044
Ago2_816-838 peptide	GenScript	N/A
Ago2_816-838(S825A) peptide	GenScript	N/A
Ago2_816-838(pS829) peptide	GenScript	N/A
Lipofectamine RNAiMAX	Invitrogen	13778150
RQ1 DNase	Promega	M6101
Ago2_816-838 peptide with heavy R838	Pierce AQUA peptide	N/A
Ago2_816-838 (pSer825) peptide with heavy R838	Pierce AQUA peptide	N/A
Ago2_816-838 (pSer829) peptide with heavy R838	Pierce AQUA peptide	N/A
Growth Factor Reduced (GFR) Matrigel	Corning	354230
Critical commercial assays		
RNeasy Plus Mini Kit	Qiagen	74143
NEBNext Poly(A) mRNA Magnetic Isolation Module	NEB	E7490
NEBNext Ultra Directional RNA Library Prep kit for Illumina	NEB	E7760
ATAC-Seq kit	ActiveMotif	53150
mirVana miRNA isolation kit	Invitrogen	AM1560
Taqman Advanced miRNA cDNA Synthesis kit	Applied Biosystems	A28007
Superose 6 Increase 10/300 Column	Cytiva	29091596
High-Capacity cDNA Reverse Transcription kit	ThermoFisher	4368813
TaqManTM Universal PCR Master Mix	ThermoFisher	4318157
CellTiter-Glo 3D	Promega	G9683
Deposited data		
RNA-Seq (colonic epithelium)	This paper	GEO: GSE189705; subseries: GSE189702
RNA-Seq (colonic tumor)	This paper	GEO: GSE189705; subseries: GSE189704

(*Continued on next page*)

Continued

REAGENT or RESOURCE	SOURCE	IDENTIFIER
RNA-Seq (T6B expressing colon)	La Rocca et al.[21]	GEO: GSE179588
ATAC-Seq (colonic epithelium and tumor)	This paper	GEO: GSE189705; subseries: GSE189699
HEAP (colonic epithelium)	This paper	GEO: GSE189705; subseries: GSE189700
HEAP (colonic tumor)	This paper	GEO: GSE189705; subseries: GSE189701
scRNA-Seq (human colonic adenoma)	Chen et al.[58]	https://data.humantumoratlas.org/
Mouse reference genome: Mus_musculus.GRCm38	Ensembl	ftp://ftp.ensembl.org/pub/release-92/fasta/mus_musculus/dna/Mus_musculus.GRCm38.dna.primary_assembly.fa.gz
Proteomics (colonic epithelium and tumor)	Brubaker et al.[34]	ProteomeXchange Consortium PRIDE partner repository: PXD013922
Phospho-proteomics (colonic epithelium and tumor)	Brubaker et al.[34]	ProteomeXchange Consortium PRIDE partner repository: PXD013922
DepMap 21Q2 Public+Score, CERES	DepMap	https://depmap.org/portal/
Experimental models: Cell lines		
Cell: MEF$^{Halo\text{-}Ago2/+}$	Li et al.[26]	N/A
Cell: Ago2$^{-/-}$ HCT116	Golden et al.[48]	N/A
Organoid: *Villin$^{CreER/+}$; Apc$^{fl/fl}$*	This paper	N/A
Organoid: *Villin$^{CreER/+}$; Apc$^{fl/fl}$; K-ras$^{LSL\text{-}G12D/+}$*	This paper	N/A
Organoid: *Villin$^{CreER/+}$; Apc$^{fl/f}$; Ankrd52$^{-/-}$*	This paper	N/A
Organoid: *Villin$^{CreER/+}$; Apc$^{fl/fl}$; K-ras$^{LSL\text{-}G12D/}$; Ankrd52$^{-/-}$*	This paper	N/A
Experimental models: Organisms/strains		
Mouse: Cg-*Ago2$^{tm1.1(DhaA*)Aven}$*/J (Halo$^{LSL\text{-}Ago2}$)	The Jackson Laboratory	JAX: 034467
Mouse: Cg-Tg(Vil1-cre/ERT2)23Syr/J (Villin^{CreER})	The Jackson Laboratory	JAX: 020282
Mouse: Tg(Fabp1-cre)1Jig/Nci (Fabp1^{Cre})	NCI Mouse Repository	Strain 01XD8
Mouse: Apc$^{tm2.1Rak}$/Nci (Apc^{2lox14})	NCI Mouse Repository	Strain 01XP3
Mouse: Kras^{tm4Tyj}/Nci (Kras$^{LSL\text{-}G12D}$)	NCI Mouse Repository	Strain 01XJ6
Oligonucleotides		
See Table S1	This paper	N/A
Recombinant DNA		
pFastBac-Csn2a1	This paper	N/A
lentiCRISPR v2	Addgene	52961
lentiCRISPR v2-Ankrd52-sgRNA1	This paper	N/A
lentiCRISPR v2-Ankrd52-sgRNA2	This paper	N/A
lentiCRISPR v2-Ankrd52-sgRNA3	This paper	N/A
pMD2.G	Addgene	12259
psPAX2	Addgene	12260
Software and algorithms		
ImageStudioLite (v5.2.5)	Li-Cor	N/A
OMERO	OMERO	https://www.openmicroscopy.org/omero/
Cutadapt (1.14)	Martin[60]	https://cutadapt.readthedocs.io/en/stable/
STAR (2.5.2b)	Dobin et al.[61]	https://github.com/alexdobin/STAR
SAMtools (1.3.1)	Danecek et al.[62]	https://www.htslib.org
seqcluster (1.2.4a7)	Pantano et al.[63]	https://github.com/lpantano/seqcluster
CLIPanalyze(0.0.10)	Li et al.[26]	https://bitbucket.org/leslielab/clipanalyze

(*Continued on next page*)

Continued

REAGENT or RESOURCE	SOURCE	IDENTIFIER
GenomicRanges (1.40.0)	Lawrence et al.[64]	https://bioconductor.org/packages/release/bioc/html/GenomicRanges.html
Rsubread (2.2.6)	Liao et al.[65]	https://bioconductor.org/packages/release/bioc/html/Rsubread.html
DESeq2 (1.28.1)	Love et al.[66]	https://bioconductor.org/packages/release/bioc/html/DESeq2.html
isomiRs (1.16.2)	N/A	https://www.bioconductor.org/packages/release/bioc/html/isomiRs.html
HOMER *de novo* motif discovery	Heinz et al.[67]	http://homer.ucsd.edu/homer/motif/
clusterProfiler (3.16.1)	Yu et al.[68]	https://bioconductor.org/packages/release/bioc/html/clusterProfiler.html
Salmon (1.4.0)	Patro et al.[69]	https://salmon.readthedocs.io/en/latest/salmon.html
Bcbio	https://doi.org/10.5281/zenodo.3564938	https://bcbio-nextgen.readthedocs.io/en/latest/contents/atac.html
CHIPseeker (1.28.3)	Wang et al.[70]	https://bioconductor.org/packages/release/bioc/html/ChIPseeker.html
GSEA (4.0.3)	Subramanian et al.[71]	https://www.gsea-msigdb.org/gsea/index.jsp
GSVA (1.38.2)	Hänzelmann et al.[72]	https://bioconductor.org/packages/release/bioc/html/GSVA.html
Seaborn	https://doi.org/10.5281/zenodo.592536	https://seaborn.pydata.org
Scipy	Virtanen et al.[73]	https://scipy.org
limma (3.52.2)	Ritchie et al.[74]	http://bioconductor.org/packages/release/bioc/html/limma.htmlhttp://bioconductor.org/packages/release/bioc/html/limma.html
Code for the analysis of ATAC-Seq (colonic epithelium)	This paper	https://doi.org/10.5281/zenodo.7994801
Code for the analysis of ATAC-Seq (colonic tumor)	This paper	https://doi.org/10.5281/zenodo.7996259
Code for the analysis of RNA-Seq (colonic epithelium)	This paper	https://doi.org/10.5281/zenodo.7996289
Code for the analysis of RNA-Seq (colonic tumor)	This paper	https://doi.org/10.5281/zenodo.7996279
Code for the analysis of RNA-Seq (T6B colon)	This paper	https://doi.org/10.5281/zenodo.7996300
Code for the analysis of Proteomics (colonic epithelium)	This paper	https://doi.org/10.5281/zenodo.7996298
Code for the analysis of Proteomics (colonic tumor)	This paper	https://doi.org/10.5281/zenodo.7996292
Code for the analysis of HEAP (colonic epithelium)	This paper	https://doi.org/10.5281/zenodo.7996283
Code for the analysis of HEAP (colonic tumor)	This paper	https://doi.org/10.5281/zenodo.7996287

RESOURCE AVAILABILITY

Lead contact

Further information and requests for resources and reagents should be directed to and will be fulfilled by the lead contact, Kevin M. Haigis (Kevin_Haigis@dfci.harvard.edu).

Materials availability

Custom reagents generated in this study are available by request from the lead contact.

Data and code availability

- All sequencing data generated in this study have been deposited in NCBI Gene Expression Omnibus (GEO). All data are publicly available as of the date of publication. Accession numbers and DOI are listed in the key resources table.
- All custom code has been deposited to GitHub and Zenodo. DOI are listed in the key resources table.
- Any additional information required to reanalyze the data reported in this paper is available from the lead contact upon request.

EXPERIMENTAL MODEL AND STUDY PARTICIPANT DETAILS

Animal models

The generation of *Ago2*$^{LSL\text{-}Halo}$ mouse was previously reported[26] and the animal is available from Jackson Laboratory (Stock No. 034467). *Villin*^{CreER} mice were obtained from Jackson Laboratory (Stock No. 020282). *Fabp1*^{Cre} (Strain 01XD8), *Apc*^{2lox14} (Strain 01XP3), and *Kras*$^{LSL\text{-}G12D}$ (1) mice were obtained from the NCI Mouse Repository. Mice were fed *ad libitum*, housed in a barrier facility with a temperature-controlled environment and twelve-hour light/dark cycle. All mice used in this study were maintained in a primarily C57BL/6 Background. All experiments involving mice ensured equal representations of both male and female animals in the control and experimental groups. All experiments were performed using sexually mature animals between 8-14 weeks of age. All experiments involving animals were approved by the Institutional Animal Care and Use Committee (IACUC) at Beth Israel Deaconess Medical Center and Dana-Farber Cancer Institute. IACUC guidelines regarding the ethical use and care of animals were followed.

Cell lines and cell culture conditions

Cell cultures were maintained in humidified incubators with 5% CO_2 at 37°C. The generation of MEFs expressing Halo-Ago2 (MEF^{HA}) was previously described.[26] Ago2$^{-/-}$ HCT116 cells expressing various FH-AGO2 variants were a generation gift from Dr. Joshua Mendell (University of Texas Southwestern Medical Center). NIH-3T3 cells were acquired from ATCC (CRL-1658). MEFs, NIH-3T3, and 293T cells are cultured in DMEM (GIBCO) containing 10% FBS, penicillin/streptomycin (100 U/mL) and L-glutamine. HCT116 cells were cultured in McCoy's 5a Medium (GIBCO) containing 10% FBS, penicillin/streptomycin (100 U/mL).

Organoid lines and culture conditions

Organoid cultures were maintained in humidified incubators with 5% CO_2 at 37°C. Matrigel (Corning #354234) was used to maintain 3D culture. Colonic organoids were established from *Villin*$^{CreER/+}$; *Apc*$^{fl/fl}$ (control) and *Villin*$^{CreER/+}$; *Apc*$^{fl/fl}$; *K-ras*$^{LSL\text{-}G12D/+}$ (experimental) animals. Loss of Apc and expression of K-Ras^{G12D} was induced via 4-hydroxytamixofen (4-OHT, 1μM, Sigma-aldrich #T176) treatment for 2 weeks to transform them into tumor organoids. The selection was achieved through depletion of Wnt and R-spondin in the culture media. These tumor organoid lines were cultured in a nutrient-rich media: Advanced DMEM/F12 (GIBCO #12634028) containing 0.5X B-27 (GIBCO #17504044), 0.5X N-2 (GIBCO #17502048), 1X Glutamax (GIBCO # 35050061), 10mM HEPES (GIBCO # 15630080), 10mM Nicotinamide (Sigma-aldrich #N0636), 500μM N-Acetylcysteine (Sigma-aldrich #A0737), 50nM [Leu15]-Gastrin I Human (Sigma-aldrich #G9145), 500nM A83-01 (Sigma-aldrich #SML0788), 10μM SB-202190 (Sigma-aldrich #S7067), 50ng/ml Recombinant human EGF (ThermoFisher #PHG0311), 1μM prostaglandin E2 (Sigma-aldrich #P0409), 100μg/ml Primocin (InvivGgen #ANT-PM-1), 10% FBS, and 100ng/ml Noggin (PeproTech #25038250UG).

METHOD DETAILS

Mouse tissue collection

Given the colon and distal ileum specific expression of *Fabp1*^{Cre}, colonic epithelium tissues from *Fabp1*$^{Cre/+}$ (control) and *Fabp1*$^{Cre/+}$; *K-ras*$^{LSL\text{-}G12D/+}$ (experimental) mice were harvested. Epithelial surface of 8-12 weeks old control and experimental mice are scraped with a razor blade and scraped tissues were flash-frozen in liquid nitrogen for RNA-Seq, ATAC-Seq, and Western blotting of endogenous proteins. Colons used for histological examinations were opened longitudinally and rolled from distal to proximal as a "swiss-roll" and fixed in 4% Formalin overnight before being embedded in paraffin.

Villin$^{CreER/+}$; *Apc*$^{fl/fl}$ (control) and *Villin*$^{CreER/+}$; *Apc*$^{fl/fl}$; *K-ras*$^{LSL\text{-}G12D/+}$ (experimental) animals were used as the colorectal cancer model in this study. Colonic tumors in 8-12 weeks old animals were induced via enema of 200μl 4-hydroxytamoxifen (4-OHT, 5mg/ml in 100% ethanol). Tumor tissues were harvested in moribund animals (1-2 weeks post-induction) by scraping the colon tumor lawn with a razor blade. Tissues used for RNA-Seq, ATAC-Seq, and Western blotting were flash-frozen in liquid nitrogen. Tumor carrying colons used for histological examinations were opened longitudinally and rolled from distal to proximal as a "swiss-roll" and fixed in 10% formalin overnight before being embedded in paraffin.

Colonic epithelium and tumor tissues with *Ago2*$^{LSL\text{-}Halo/+}$ were collected for HEAP and Halo-Ago2 characterization experiments. For HEAP, the collected colonic epithelium and tumor tissues were UV-crosslinked before being flash-frozen in liquid nitrogen.

Collected tissue from each animal was minced and resuspended in ice-cold PBS in a 6cm petri-dish. Tissue suspension was cross-linked in a UV Stratalinker 2400 at 400mJ/cm^2 three times on the ice. The tissue was then pelleted, and flash frozen for HEAP.

Western blotting

Primary antibodies against the following targets were used for Western blotting: Ras (Millipore #05-516, 1:1000), Ras^{G12D} (Cell Signaling Technology (CST) #14429, 1:1000), K-Ras (Millipore #OP-24, 1:100, specificity validated by Waters et al.[75]), Gapdh (CST #5174, 1:1000), Erk (CST #4696, 1:1000), p-Erk(Thr202/Tyr204) (CST #4377, 1:1000), Vinculin (CST #13901, 1:1000), Mek (CST #4694, 1:1000), p-Mek(Ser217/221) (CST #9121, 1:1000), Ago2 (CST #2897, 1:1000), HaloTag (Promega #G9211, 1:1000), Tubulin (Calbiochem #CP06, 1:10,000), Tnrc6a (Bethyl Laboratories #A302-329A-M, 1:1000), Csnk1a1 (Santa-Cruz Biotechnology #sc-74582, 1:1000), Csnk2a1 (CST #2656, 1:1000), Ppp6c (Abcam #ab131335, 1:1000), Ankrd52 (LSBio #LS-C483018, 1:1000), Hsp90ab1 (CST #5087, 1:1000), p-Hsp90ab1(Ser226) (LSBio #LS- C359019, 1:1000), CK2 phospho-motif (CST #8738, 1:1000), Csnk1d (Santa-Cruz Biotechnology #sc-514942, 1:1000). The following secondary antibodies were used: Alexa Fluor Plus 800 Goat anti-Rabbit IgG (Invitrogen #A32735) and Alexa Fluor 680 Goat anti-Mouse IgG (Invitrogen #A21058).

Tissue samples used for Western blotting were powderized. Bioplex lysis buffer (Bio-rad #171304011) with 1X cOmplete^{TM} EDTA-free protease inhibitor cocktail (Millipore-Sigma #11873580001) was used to lyse the samples. Sample lysates were incubated at 4°C with gentle rocking for one hour before being clarified through centrifugation. Protein concentrations of each sample were determined by BCA assay before being subjected to SDS-PAGE followed by blotting with the indicated antibodies. Intercept (PBS) blocking buffer and antibody diluent were used (Li-Cor #927-76003). Diluted primary antibodies were incubated with the blots overnight at 4°C. Secondary antibodies were incubated at room temperature for 1 hour. Signal was detected using Li-Cor Odyssey CLX (LI-COR Biotechnology, Lincoln, Nebraska, USA) and analyzed using ImageStudioLite (version 5.2.5). Phospho signals were normalized to total protein levels. All protein signals were normalized to K-Ras^{WT} or control samples.

Histological characterizations

Antibodies

Primary antibodies against the following targets were used for immunohistochemistry (IHC) or immunofluorescence (IF): Ras^{G12D} (CST #14429, 1:50), Ki67 (CST #12202, 1:400), p-Erk(Thr202/Tyr204) (CST #9101, 1:250), Lysozyme (ThermoFisher # RB-372-A1, 1:200), E-Cadherin (BD Biosciences #610181, 1:750), β-catenin (CST #9562, 1:800). Secondary antibodies used in IHC was Envision+ HRP conjugated anti-rabbit polymers (Agilent #K400311-2). Secondary antibodies used in IF included Alexa Fluor 647 Goat anti-Rabbit IgG (Invitrogen #A21244), Alexa Fluor 488 Goat anti-Rabbit IgG (Invitrogen #A11034), and Alexa Fluor 594 Goat anti-Mouse IgG2a (Invitrogen #A21135).

H&E

Tissue sections (5μm) were deparaffinized in a standard Histo-Clear (National Diagnostics #HS2001GLL) and ethanol series. Standard hematoxylin and eosin standing protocol were followed.

Immunohistochemistry and immunofluorescence

Tissue sections (5μm) were deparaffinized in a standard Histo-Clear (National Diagnostics #HS2001GLL) and ethanol series. Deparaffinized tissue sections (5μm) were subjected to antigen retrieval using target retrieval solutions of citrate pH6.1 (Dako #S1699) or pH9 (Dako #S2367). For IHC, tissue sections were incubated with Peroxidase and Alkaline Phosphatase Blocking Reagent (Agilent #S200389-2) for 5 minutes at room temperature following antigen retrieval. Sections were then incubated with Protein Block, Serum-free (Dako #X0909) for 20 minutes at room temperature. Primary antibodies were diluted in Antibody Diluent (Agilent #S302283-2) and incubated with tissue sections overnight at 4°C. Following primary antibody application, Envision+ HRP conjugated anti-rabbit polymers (Agilent #K400311-2) were applied to the sections for 30 minutes at room temperature. Liquid DAB+ substrate (Agilent # K346811-2) was used to develop signals of the target protein. Samples were mounted with Permount (Fisher #SP15-100). Slide images were acquired using the Olympus VS120 slide scanner (Olympus Life Sciences). Image processing was completed with OMERO (https://www.openmicroscopy.org/omero/). For IF, tissue sections were incubated with protein block (DAKO) for 20 minutes at room temperature following antigen retrieval. Primary antibodies were diluted in Antibody Diluent (DAKO) and incubated with slides overnight at 4°C. Secondary antibodies and DAPI (BD Biosciences #564907, 1:1000) were diluted in Antibody Diluent (Dako) and centrifuged at max speed in a tabletop centrifuge at room temperature for 5 minutes to remove fluorophore aggregates. Diluted secondary antibody/DAPI solution was then applied to tissue sections for 1 hour at room temperature shielded from light. Samples were mounted with Prolong Diamond (ThermoFisher # P36961). Slide images were acquired using the Olympus VS120 slide scanner and processed using OMERO.

HEAP library preparation

UV-crosslinked and flash-frozen pellets of Halo-Ago2 expressing colonic epithelium and tumor +/- K-Ras^{G12D} were used for HEAP. For the colonic epithelium HEAP, three samples each were prepared from K-Ras^{WT} or K-Ras^{G12D} tissues. Due to K-Ras^{G12D} induced hyperplasia in the colon, tissue samples from twelve K-Ras^{WT} mice or three K-Ras^{G12D} mice were pooled into each sample to ensure the mass balance of tissue inputs. For the colonic tumor HEAP, three samples each were prepared from K-Ras^{WT} or K-Ras^{G12D} tissues, with three K-Ras^{WT} mice or three K-Ras^{G12D} mice pooled into each sample.

The preparation of HEAP included HEAP and Input Control (IC) libraries was performed as previously described.[26] To briefly summarize, frozen tissue sample pellets were powderized, weighed, and pooled to ensure the mass balance of inputs. Tissue powders were then lysed in Mammalian lysis buffer (Promega #G9381) with 1X Protease Inhibitor Cocktail (Promega #G6521). Sample lysates were then treated with sequential DNase (Promega #M610A) and mild RNase (ThermoFisher #EN0531) digestion. Lysates were passed through a 26-gauge needle and clarified via centrifugation. 2% of cleared input lysate was saved from each sample for IC library construction. The remaining lysates were diluted in TBS (3:7) and subjected to Halo-Ago2 pulldown using the HaloLink Resin (Promega #G1914). Ago2:RNA complexes on the resin were treated with Alkaline phosphatase (Promega #M182A) to dephosphorylate RNA 3' end before 3' RNA linker ligation using T4 RNA ligase (NEB #M0204). T4 PNK (NEB #M0201) treatment was then performed to phosphorylate RNA 5' end before RNA isolation and 5' RNA linker ligation with T4 RNA ligase. RNA isolation was done following protease K digestion of the Ago2 protein to release capture mRNA and miRNA. RNA was then purified through phenol-chloroform precipitation. Ligated 5' linker contained unique random barcodes that were used to remove read duplicates from PCR in subsequent analysis. RT PCR was performed on purified RNA with both 3' and 5' linkers ligated using SuperScript III Reverse Transcriptase (Invitrogen #18080044). Diagnostic PCR was performed on each sample to determine the optimal cycles of amplification. For colonic epithelium HEAP, 21 cycles were used for all samples. For colonic tumor HEAP, 19 cycles were used for all samples except one K-Ras^{WT} and one K-Ras^{G12D} sample were amplified with 21 cycles. Amplified samples were subjected to TBE-Urea PAGE. For each sample, a prominent band at ~60bp was gel extracted as it contained Ago2-bound miRNA and was subsequently prepared and sequenced as the miRNA library. DNA from 75-200bp was gel extracted as it contained Ago2-bound mRNA and was subsequently prepared and sequenced as the HEAP library. Index PCR was performed on Isolated miRNA and mRNA samples using previously described custom index primers[26] and modified 5' primer DSFP5-PE (AATGATACGGCGACCACCGAGATCTACACCTA TGGATACTTAGTCAGGGAGGACGATGCGG), ensuring sequencing compatibility with the NextSeq 500 platform. For the IC library, saved input lysate was treated with Alkaline Phosphatase and T4 PNK and underwent 3' and 5' linker ligation as described above. Ligated RNA was extracted using Dynabeads™ MyOne™ Silane (Invitrogen #37002D) and purified with phenol-chloroform precipitation. RT, diagnostic, and amplification PCR was performed as described above. DNA from the 60-200bp range of the TBE-Urea PAGE gel was gel extracted as IC samples. Index PCR was performed for IC samples as described above. Indexed miRNA, HEAP, and IC libraries were further size selected and purified via TBE PAGE. Single-read sequencing of the purified libraries was performed on the NextSeq 500 platform (Illumina) with High Output and 75 cycles using custom sequencing primer SSP1 (CTATGGATACTTAGTCAGGGAGGACGATGCGG).

RNA-seq library preparation

Flash-frozen colonic epithelium and tumor tissues +/- K-Ras^{G12D} were powderized in liquid nitrogen using a tissue homogenizer. RNeasy Plus Mini Kit (Qiagen #74143) was used to extract RNA from tissue following the manufacturer's instructions. RNA concentration and quality were determined by Agilent Bioanalyzer/TapeStation. 1μg of RNA with RIN > 7 from each sample was used as input for RNA-Seq library preparation. Poly-A enrichment was performed using NEBNext Poly(A) mRNA Magnetic Isolation Module (NEB #E7490). RNA-Seq library was prepared using NEBNext Ultra Directional RNA Library Prep kit for Illumina (NEB #E7760) following the manufacturer's instructions. Quality control of the libraries was done using Agilent TapeStation and qPCR. Single read sequencing of the libraries was done on NextSeq 500 (Illumina) with High Output and 75 cycles.

ATAC-seq library preparation

20-30mg of flash-frozen colonic epithelium and tumor tissues +/- K-Ras^{G12D} were used as input without being powderized. Tissue samples were minced on ice in ice-cold PBS before lysis and nuclei isolation. 100,000 nuclei from each sample were used as input for tagmentation. Libraries were constructed using the ATAC-Seq kit (ActiveMotif #53150) following the manufacturer's protocol. Quality control of the libraries was done using Agilent TapeStation and qPCR. Pair-end sequencing of the libraries was done on NovaSeq 6000 (Illumina) with V1.5 S1 100 cycles kit (50 cycles each end).

miRNA qPCR

30mg of powdered frozen tissues were used as input for total RNA extraction (mRNA + small RNAs) using the mirVana miRNA isolation kit (Invitrogen #AM1560) following manufacturer's protocol. miRNA cDNA was synthesized using Taqman Advanced miRNA cDNA Synthesis kit (Applied Biosystems #A28007). Taqman Advanced miRNA Assays were performed using synthesized cDNA and the following Taqman probes: miR-200b-3p (mmu482918_mir), miR-200c-3p (mmu482938_mir), miR-429-3p (mmu481162_mir), miR-29a-3p (478587_mir), miR-29b-3p (mmu481300_mir), miR-29c-3p (mmu479229_mir). miR-186-5p (mmu480966_mir) was recommended and selected and loading control.

Halo-Ago2 pull-down qPCR

Powdered colonic epithelium and tumor tissues +/- K-Ras^{G12D} were used as inputs. This is performed using a modified version of a previously published protocol.[48] 50mg of tissue was lysed on ice in 500μl of G buffer (25mM Tris pH8, 150mm NaCl, 2mM $MgCl_2$, 0.5% IGEPAL-CA630, 1mM DTT) with 1X Protease Inhibitor (Promega # G6521), 250U/ml RNasin Ribonuclease Inhibitor (Promega #N2515), and 10mM sodium pyrophosphate. Lysis was performed by gentle grinding of tissue in lysis buffer to avoid complex disassembly. Lysates were cleared by centrifugation and protein concentrations of all samples were normalized following BCA assay to ensure equal protein

input. 4% lysate was saved as input from each sample, with half designated for qPCR as input and half used for Western blotting. Lysates were incubated with HaloLink resin (Promega #G1914) overnight at 4°C. Lysates with resin were then spun down to remove the unbound fraction, with 2% saved for Western blotting. Resins were washed with 4 short washes (inverting the tube) and 1 long wash (rotated for 5 minutes at room temperature) using G buffer. Ago2:RNA complex on the resin was recovered by HaloTEV protease cleavage (Promega #G6602). 80% of the eluate was used for RNA extraction and qPCR and the remaining 20% was used for Western blotting. 2% input, 2% unbound, and 20% eluate was used for WB and the amounts of Ago2 recovered from each sample were used to normalize the amount of RNA pulled down by Ago2. RNA was extracted from 2% input and 80% eluate and qPCR was performed using the following Taqman probes: Sema7a (Mm01171206_g1), Dhrs9 (Mm00615706_m1), Egfr (Mm01187858_m1), Cldn4 (Mm01196224_s1), Ctsd (Mm00515586_m1), Abhd17b (Mm01197077_m1), Nt5c1a (Mm01192250_m1), S100a16 (Mm00509523_g1), Fth1 (Mm04336020_g1), B2m (Mm00437762_m1), Ly6g (Mm07306432_mH), Abcb1a (Mm00440761_m1), Gsta4 (Mm00494803_m1), Tns4 (Mm00553421_m1), S100a14 (Mm04206817_g1), Rplp2 (Mm03059047_gH), Usp24 (Mm01256454_m1), Itga2 (Mm00434371_m1), Myof (Mm00621780_m1), Gca (Mm00521120_m1), Pisd (Mm00624052_m1).

Halo-Ago2 pull-down

Powdered colonic epithelium and tumor tissues +/- K-Ras^{G12D} were used as inputs. Pull down was performed similarly to the Halo-Ago2 pulldown qPCR experiment using K buffer (20mM Tris pH 7, 5mM EDTA, 150mM NaCl, 1% Triton X100, 1mM DTT), which was previously shown to support Ras-Ago2 association.[43,76] K buffer with 1X protease inhibitor (Promega # G6521) and 10mM sodium pyrophosphate as phosphatase inhibitor was used for tissue lysis. Lysate inputs were normalized. 3% input, 3% unbound, and all eluates were used for Western blotting. Tnrc6a in the eluates were normalized to Ago2.

Size exclusion chromatography

Frozen cell pellets and powdered colonic epithelium and tumor tissues +/- K-Ras^{G12D} were used as inputs. RISC analysis using this method has been described previously.[20] To briefly summarize, cell pellets or 50mg of tissue was lysed in S6 buffer (10mM Tris pH 7.5, 150mM NaCl, 2.5mM $MgCl_2$, 0.01% Triton X100, 1mM DTT) with 1X protease inhibitor (Promega # G6521), and 1X phosphatase inhibitor cocktail 2&3 (Sigma #P5726 & #P0044). Lysis was performed by gentle grinding of tissue in lysis buffer to avoid RISC disassembly. Lysates were cleared by centrifugation. Protein concentrations were evaluated to ensure similar input in each chromatography experiment and 2% lysate was saved as input. 0.5mg of lysate protein was loaded onto the Superose 6 Increase 10/300 Column (Cytiva #29091596) using the ÄKTA Pure platform (Cytiva) with 0.1ml/minute flow rate and S6 buffer as the running buffer. 1ml fractions were collected. Proteins in each fraction were TCA precipitated before being re-suspended in PBS and prepared for SDS-PAGE and Western blotting.

RT-qPCR

Powdered colonic tissues +/- K-Ras^{G12D} were used for RNA extraction. RNeasy Plus Mini Kit (Qiagen #74143) was used to extract RNA from tissue following the manufacturer's instructions. cDNA was synthesized using High-Capacity cDNA Reverse Transcription kit (ThermoFisher # 4368813) with 1μg of RNA from each sample as inputs. qPCR was performed using TaqManTM Universal PCR Master Mix (ThermoFisher # 4318157) with the following probes: Csnk1a1 (Mm00521599_m1), Csnk2a1 (Mm00786779_s1), Gapdh (Mm99999915_g1).

Protein expression and purification

Full-length, mouse CsnK2a1 (CK2) was cloned into pFastBac with a TEV-cleavable, N-terminal 6xHis tag and verified via Sanger sequencing. Recombinant baculovirus was prepared and used to infect Sf9 insect cells. Post infection, cells were pelleted and re-suspended in lysis buffer composed of 50 mM Tris pH 8.0, 300 mM NaCl, 1 mM tris(2-carboxyethyl) phosphine (TCEP), 0.2 mM phenylmethylsulfonyl fluoride (PMSF), and 5% glycerol. Cells were lysed via sonication before ultracentrifugation at >200,000 g for 1 h. The resulting clarified supernatant was flowed through Ni-NTA resin, and the resin was washed with lysis buffer supplemented with 40 mM imidazole before elution with lysis buffer containing 200 mM imidazole. Eluted CK2 was further purified via size exclusion chromatography on a prep-grade Superdex S200 column in 50 mM Tris pH 8.0, 300 mM NaCl, 1 mM TCEP, and 5% glycerol. Fractions containing CK2 were combined and concentrated to approximately 1 mg/mL and flash frozen.

In vitro peptide phosphorylation

Wild-type and S825A peptides spanning residues 816-838 of mouse Ago2 were synthesized (GenScript, NJ, USA). In vitro phosphorylation contained 100 μM peptide and 5 μM purified CK2 in 50 mM Tris pH 8.0, 300 mM NaCl, 1 mM TCEP, 10 mM MgCl2, and 5% glycerol. Reactions were initiated with 1 mM ATP and allowed to proceed overnight at room temperature. Dot blot was performed by applying 2.5μl of each peptide/kinase sample per dot on a nitrocellulose membrane. Membrane was air-dried for 1 hour at room temperature after sample application. Standard western blotting procedure was followed afterwards. Custom antibody developed for detecting p-Ago2(Ser825) was used as primary antibody at 1:500 dilution. Mass spectrometry (MS) based detection of Ago2 (Ser825) phosphorylation was performed using *in vitro* phosphorylation reactions described above but with wild-type (naked) or p-Ago2(Ser829) peptide. Following incubation with ATP and CK2, peptides were diluted to 8M in Tris-HCl and desalted over a C18 column. Samples were then dried via vacuum centrifugation and resuspended in 5% acetonitrile (MeCN)/1% FA and analyzed

on an Ultimate 3000 RSLCnano system coupled to an Orbitrap Eclipse mass spectrometer (Thermo Fisher Scientific). The peptides were separated across a 30-min gradient of 6 to 95% MeCN in 1% FA over a 50-cm C18 column (ES803A, Thermo Fisher Scientific) and electrosprayed (2.15 kV, 300°C) into the mass spectrometer with an EasySpray ion source (Thermo Fisher Scientific). Precursor ion scans (380 to 1,500 m/z) were obtained in the orbitrap at 120,000 resolution in profile (RF lens % = 30, Max IT = 200 ms). Fragment ion scans were collected with a 0.5 m/z isolation window, HCD (higher-energy C-trap dissociation) at 30% NCE (normalized collision energy), 30,000 orbitrap resolution, and with charge states ranging from $z = 1+$ to $z = 5+$. Proteome Discoverer 2.4 (Thermo Fisher Scientific) was used for .RAW file processing and controlling peptide false discovery rates. MS/MS spectra were searched against a Uniprot human database (January 2021) with both the forward and reverse sequences, as well as known contaminants. Peptide sequence and phosphorylation site localization were confirmed from fragment ion spectra and retention time, and precursor abundances were quantified from extracted ion chromatograms and used to determine percent phosphorylation of Ser825 and Ser829 across samples. Experiments were conducted in triplicate.

Custom antibody development

Custom antibody against p-Ago2(Ser825) was developed by ThermoFisher. Rabbits were inoculated with Ago2 (819-830) peptide (C-DKEHD(pS)AEGSH-amide) with phosphorylated Ser825 and KLH conjugation. Serum was purified from animal blood collected 72 days post inoculation. Polyclonal antibodies against Ago2(Ser825) phosphorylation was further purified by enrichment of antibodies against p-Ago2(Ser825) peptide and negatively selection against non-phosphorylated Ago2(819-830) peptide. Purified antibody specificity was tested against p-Ago2(Ser825) peptide relative to the control non-phosphorylated Ago2 peptide using dot blot. Custom antibody-based detection of p-Ago2(Ser825) from endogenous lysate was also attempted but yielded no clear signal compared to the background due to antibodies' low affinity to p-Ago2(Ser825) (Data not shown). Therefore, custom antibody was only used for detecting p-Ago2(Ser825) in *in vitro* phosphorylation experiments.

Antibody validation

For validation of antibodies detecting protein, siRNA-mediated knockdown was performed in NIH-3T3 cells. Cells were transfected with either scramble control siRNA or siRNAs targeting genes of interest using Lipofectamine RNAiMAX (Invitrogen #13778150). Cells were harvested 96 hours post-transfection, pelleted, and flash-frozen for protein extraction. Cell pellets were lysed in RIPA buffer with 1X cOmplete^{TM} EDTA-free protease inhibitor cocktail (Millipore-Sigma #11873580001) and 1X Phosphatase inhibitor cocktail 2&3 (Sigma #P5726 & #0044). Lysates were subjected to SDS-PAGE and Western blotting analysis. siRNA used are: si-Csnk1a1 (Dharmacon # L-062865-00-0005), si-Csnk2a1 (Dharmacon # L-058653-00-0005), si-Ago2 (L-058989-01-0005).

To validate phospho-specific antibodies, MEF cell lysates were aliquoted and lambda phosphatase (NEB #0753) treatment was performed using one aliquot following the manufacturer's instruction. Control and lambda phosphatase treated lysates were subjected to SDS-PAGE and Western blotting analysis.

CRISPR knockout of Ankrd52

CRISPR-Cas9 mediated genetic knockout of Ankrd52 was carried out in MEF^{HA} cells. Three sgRNAs targeting Ankrdr52 exon3 (gRNA1: GATGGGGACATCGCCTACGT, gRNA2: GTAGGCAGCAGCATGCAATG, gRNA3: CTGACATCAGTAGCAACTGG) were cloned into lentiCRISPR v2 (LCV2) backbone (Addgene #52961). Lentivirus production was done in 293T cells with co-transfection of LCV2-Ankrd52-sgRNAs with pMD2.G (Addgene #12259) and psPAX2 (Addgene #12260). Viral supernatant containing was was filtered and transferred to MEF^{HA} cells with 8μg/ml polybrene. Infected cells were selected with 2μg/ml puromycin for 2 weeks before single cell cloning and Western blotting validation of complete knockout.

Halo-Ago2 purification followed with MS

To purify Ago2 from MEF^{HA} cells +/- Ankrd52, cells were cultured in 150mm dishes. For each line, 8 confluent 150mm dishes were scraped in ice-cold PBS, pelleted, and flash-frozen in liquid nitrogen as input. Lysis of each pellet was performed in 5ml of Mammalian lysis buffer (Promega #G9381) with 1X Protease Inhibitor (Promega # G6521) and 50mM NaF as phosphatase inhibitor. Lysates were incubated on ice for 15 minutes before RQ1 DNase treatment (Promega #M6101). Lysates were then passed through a 26-gauge needle to reduce viscosity and diluted 1:4 in purification buffer (1mM DTT, 0.005% IGEPAL-CA630 in PBS). Diluted lysates were cleared by centrifugation. BCA was performed on cleared lysates to normalize input protein amount across all samples. Lysates were then incubated with HaloLink resin (Promega #G1914) overnight at 4°C. Resin with Ago2 was recovered after removal of the unbound fraction after incubation. Samples were washed with wash buffer (500mM NaCl, 0.005% IGEPAL-CA630, 5mM EDTA, 5mM EGTA, 1mM DTT, in PBS) three times by mixing at 1200rpm for 10 minutes on a thermal shaker at room temperature. Resins were then washed with purification buffer three times by mixing at 1200rpm for 5 minutes on a thermal shaker at room temperature. Purified Ago2 was recovered from the resin through HaloTEV protease cleavage (Promega #G6602) that release Ago2 from the HaloTag. Purified Ago2 was TCA precipitated and submitted to the Taplin Mass Spectrometry Facility at Harvard Medical School for quantitative MS to measure Ago2 as well as Ser825/829 phosphorylation. Relative quantification of purified Ago2, as well as Ago2 phosphorylation on the Ser825/829 site, was achieved by spiking in synthetic Ago2(Y816-R838) peptides with a heavy Arginine during the MS run, both naked and with phosphorylations on Ser825 or Ser829 positions (Pierce AQUA peptide).

Organoid viability assay

Organoids were cultured using Growth Factor Reduced (GFR) Matrigel (Corning #354230) in minimal organoid media: Advanced DMEM/F12 containing 1X Glutamax, 100μg/ml Primocin, 10μM HEPES, 1X B-27, 1X N-2, 1mM N-Acetylcysteine, 0.5ng/ml EGF, 100ng/ml Noggin. K-Ras^{WT} and K-Ras^{G12D} colonic tumor organoids +/- Ankrd52 were trypsinized into single cells and re-suspended in 10% GFR Matrigel in minimal media to a concentration of 20,000 cells/ml. Cell suspension was then plated into 384-well ultra-low attachment plate with black wall and clear bottom with 400 cells/20μl/well. 48 replicate wells were plated for each line and empty control. Three replicate plates were plated each round and each plate was used for viability readout using EVOs microscope and CellTiter-Glo 3D (Promega #G9683) every 24 hours following manufacturer's protocol.

QUANTIFICATION AND STATISTICAL ANALYSIS

Histological measurements

All measurements from histological data were carried out on OMERO. Crypt height was measured for each crypt of the distal colonic epithelium +/- K-Ras^{G12D}. At least 200 crypts were measured from each section. Ki67+ height was measurement from the base of the crypt to the tip of the Ki67+ zone.

HEAP processing

Barcode and adaptor removal

The first 7nt of each read contained the 6nt random barcode plus the nucleotide "G" from the 5' linker ligated to the RNA samples. They were removed, tagged with "UMI_" in front, and appended to the read name of each read. These tags were later used to collapse the aligned reads for PCR duplicate removal.

Cutadapt (1.14) was used to remove the 3' adaptor with the sequence 5'-GTGTCAGTCACTTCCAGCGGGATCGGAAGAGCACACGTCTGAACTCCAGTCAC-3'. Reads with a quality score lower than 20 and read length shorter than 18nt after the adaptor removal were excluded from further analysis.

Read alignment and PCR duplicate removal

For HEAP and IC libraries, STAR (2.5.2b) was used to align barcode and adaptor removed reads with Ensembl mm10 genome (Mus_musculus.GRCm38) as the reference. Multi-mapped reads and reads with more than 5 mismatches were discarded from the alignment. Chromosome name, strand information, and starting position were used to identify reads aligned to the same position. Reads with identical 7nt barcodes and mapping locations were considered PCR duplicates and were collapsed to a single unique read. Unique reads and their mapping positions were output to a separate 'BAM' file, indexed using SAMtools (1.3.1), and used for subsequent peak calling.

For miRNA libraries, barcode and adaptor removed reads were collapsed based on the UMI tags to remove PCR duplicates and identify unique miRNA reads using the 'collapse' function from seqcluster (1.2.4a7). miRNA alignment and counting were achieved with the 'miraligner' function of seqcluster using hairpin and mature miRNA sequences from miRbase (version 22.1) as the reference database.

HEAP analysis

Peak calling and annotation

Peak (Ago2 binding site) calling was performed using the 'findPeaks' function of the CLIPanalyze (https://bitbucket.org/leslielab/clipanalyze) package with the following parameters: exclude.mirna.peaks = TRUE, genome = "mm10", bandwidth = 60, count.threshold = 5, count.exons.only = FALSE. Peaks were annotated with associated genes by overlapping with 3'UTR, 3'UTR-adjacent, 5'UTR, 5'UTR-adjacent, exon, intron, intergenic, in that order. In addition to the standard peak data output, genomic locations of peaks were annotated in a separate 'BED' file.

For colonic epithelium, a full set of peaks were generated comparing three independent HEAP with three matching IC libraries for both K-Ras^{WT} and K-Ras^{G12D} samples. For colonic tumors, a full set of peaks were generated comparing six independent HEAP with six matching IC libraries for both K-Ras^{WT} and K-Ras^{G12D} samples. A separate peak data table was generated for K-Ras^{WT} colonic epithelium, K-Ras^{G12D} colonic epithelium, K-Ras^{WT} colonic tumor, and K-Ras^{G12D} colonic tumor. Peaks from all four conditions were further filtered by width > 20nt, $\log_2$FC(HEAP vs IC) > 0, average HEAP count > 10, and padj (HEAP vs IC) < 0.05 to acquire the final list of active Ago2 bound target locations. Analysis result is included in Data S1.

Merging peaks and analysis

Peaks called from K-Ras^{WT} and K-Ras^{G12D} separately were merged to allow for differential Ago2-binding comparison. Peak calling was not performed by grouping HEAP and IC libraries from K-Ras^{WT} and K-Ras^{G12D} samples due to the potential loss of K-Ras^{WT} and K-Ras^{G12D} specific peaks. Instead, the unfiltered lists of peaks output from the ''findPeaks'' functions from K-Ras^{WT} and K-Ras^{G12D} samples were merged using GenomicRanges (1.40.0). Read counts in merged peaks were acquired using the ''featureCount'' function from Rsubread (2.2.6) across K-Ras^{WT} and K-Ras^{G12D} samples. For global normalization, read counts in genes outside of the peaks were used as those were likely reads of RNA non-specifically bound to the resin during the Halo-Ago2 pulldown. Under the assumption that global total RNA abundance remained stable between K-Ras^{WT} and K-Ras^{G12D} samples, RNAs non-specifically bound to the resin during pulldown should also remain stable +/- K-Ras^{G12D}. Read counts in all exons were acquired using

"featureCount" and counts in any gene that contained HEAP peaks were removed from the count table. Counts in genes outside of peaks were normalized using DESeq2 (1.28.1) and their sizeFactors were extracted for normalization of the count data in merged peaks. Merged peaks were filtered by overlapping merged peaks with filtered peaks from the K-Ras^{WT} or K-Ras^{G12D} alone analysis. Filtered merged peaks were used for subsequent analysis. Differential Ago2 binding analysis was performed through DESeq2 using HEAP counts in the filtered merged peaks comparing K-Ras^{G12D} with K-Ras^{WT} samples. sizeFactors estimated using counts in genes outside of peaks were used for normalization of the counts in filtered merged peaks.

Ago2-bound miRNA abundance analysis

Output '.mirna' files from 'miraligner' were processed with isomiRs (1.16.2) to plot isomiR abundance and to perform differential Ago2 bound abundance analysis. miRNA family information was acquired from the TargetScan website (http://www.targetscan.org/mmu_80/mmu_80_data_download/miR_Family_Info.txt.zip). Read counts of miRNA members of the same family were aggregated. Analysis result is included in Data S2.

Peak-miRNA association

Mature miRNA family seed sequences were acquired from TargetScan and used to generate 8mer, 7merA1, 7merM8, and 6mer seed match sequences. miRNA families with mean counts > 200 were considered for association with HEAP peaks. Sequences of HEAP peaks were mapped with seed matches from selected miRNA families and peaks were associated with miRNA families based on 8mer, 7merA1, 7merM8, or 6mer matches in that order.

Benchmarking HEAP targets using the human TargetScan database

miRNA families were ranked by their number of associated HEAP targets in descending order. Top n families with associated targets cumulatively accounting for more than 80% of all identified HEAP targets were defined as "active". 34 miRNA families were considered "active" using this criteria: let-7-5p/miR-98-5p, miR-15-5p/16-5p/195-5p/322-5p/497-5p, miR-29-3p, miR-200-3p/429-3p, miR-17-5p/20-5p/93-5p/106-5p, miR-24-3p, miR-194-5p, miR-27-3p, miR-103-3p/107-3p, miR-196-5p, miR-23-3p, miR-26-5p, miR-19-3p, miR-25-3p/32-5p/92-3p/363-3p/367-3p, miR-30-5p/384-5p, miR-484, miR-141-3p, miR-130-3p/301-3p, miR-22-3p, miR-96-5p, miR-182-5p, miR-181-5p, miR-148-3p/152-3p, miR-205-5p, miR-7-5p, miR-34-5p/449-5p, miR-132-3p/212-3p, miR-30a-3p/30d-3p/30e-3p, miR-31-5p, miR-194-2-3p/6926-5p/7055-5p, miR-423-5p, miR-141-5p/6769b-3p, miR-21ac-5p, miR-139-5p.

500 genes were randomly sampled from each of the three sets: HEAP 3'UTR targets (miRNA target genes identified using HEAP with target site in the 3'UTR), Human TargetScan (miRNA target genes in human TargetScan database), Whole Transcriptome (all detected genes in colonic tissue transcriptome). Only HEAP targets with target sites in the 3'UTR were included in this analysis as the TargetScan database only considers miRNA targeting in the 3'UTR. Random sampling within each set was repeated 10,000 times. Within each group of 500 sampled genes, the fraction of conserved targets was calculated as n(targets of active miRNA families in human TargetScan) / n(targets in human TargetScan).

HOMER de novo *motif discovery*

Filtered peaks from K-Ras^{WT} alone, K-Ras^{G12D} alone, or merged analysis were used for motif discovery. Unbiased motif enrichment analysis was first performed in HEAP peaks. 'calculateKmerBackground' function of CLIPanalyze (0.0.10) was used to determine background kmer frequencies (k = 7) in the exons of genes with any unfiltered HEAP signal. Kmers enriched in the filtered HEAP peaks were determined using the "findKmerEnrich" function of CLIPanalyze using pre-determined background kmer frequencies. The exact positions of the top 50 7mers found from the unbiased motif enrichment analysis were located and the 15bp regions around the 7mers were subjected to HOMER *de novo* motif discovery. Background regions were set as the 15bp window shifted 100 and 200bp on both sides of the 7mers, excluding any overlap with other HEAP peaks.

KEGG enrichment analysis

Gene targets associated with each miRNA family were used for KEGG enrichment analysis to identify pathways specifically targeted by certain miRNA. Background of the enrichment was set to all genes. 'enrichKEGG' function of clusterProfiler (3.16.1) was used to perform the analysis. Significant pathways were selected based on p.adjust < 0.05. Analysis result for all available kinases is included in Data S3.

mRNA half-life analysis

The half-life of HEAP target genes was acquired from a previous study.[77] RNAs were ranked based on their half-life and genes within the top and bottom 10% were selected. LFC of HEAP peaks associated with these RNAs were selected and the cumulative distribution of them were plotted.

RNA-seq processing and analysis

Quality control of the sequencing was done using FastQC (0.11.5) and Qualimap (2.2.2). Salmon (1.4.0) pseudo-aligner was used for sequence mapping and transcript read counting with Ensembl mm10 genome (Mus_musculus.GRCm38) as reference. Differential gene expression analysis was performed using DESeq2 (1.28.1) with '.sf' files generated from Salmon as inputs. For the published T6B colon RNA-Seq dataset (GSE179588), the raw count data matrix was processed with DESeq2 for subsequent differential expression analysis. Analysis result is included in Data S2.

PAGE Z-score calculation

Parametric Analysis of Gene-set Enrichment (PAGE) z-score was calculated using a previously described approach.[33] Transcriptomic and proteomic data comparing RNA/proteins in K-Ras^{G12D} tissues against K-Ras^{WT} tissues were used as input. Log fold

changes (LFCs) of the selected subset of genes (targets of each miRNA family) were evaluated against the background LFC. Z-score = (Sm - μ) x $m^{1/2}$ / SD, where Sm represents mean LFC of selected genes, m stands for the number of selected genes, μ and SD show mean and standard deviation of LFCs for all genes in the dataset. Positive/negative z-scores indicated up/downregulation of selected genes compared to the background.

MS-based proteomic and phospho-proteomic analysis

Proteomics and phospho-proteomics data of colonic epithelium and tumor were acquired from ProteomeXchange Consortium PRIDE partner repository: PXD013922. Differential analysis was performed comparing K-Ras^{G12D} with K-Ras^{WT} tissues with unpaired t-tests to obtain p values. Benjamini-Hochberg procedure was employed to correct for multiple hypotheses to obtain q values. Proteins and phosphorylations with $p < 0.05$ and $q < 0.1$ were considered significantly dysregulated. For each phosphorylation site, standard log fold change was calculated and scaled to the log fold change of the protein in the proteomic dataset. Analysis result is included in Data S2.

ATAC-seq processing and analysis

FastQC (0.11.5) was used to examine the sequencing quality of the libraries. Bcbio (https://bcbio-nextgen.readthedocs.io/en/latest/contents/atac.html) ATAC-Seq pipeline on the Harvard Medical School O2 high performance computing cluster was used for sequencing processing, alignment, and peak calling. Peaks were merged across samples +/- K-Ras^{G12D} within the same tissue context (epithelium or tumor) using '.narrowPeak' outputs from the nucleosome-free fraction of each sample. Peaks within 500bp of each other were merged as a single peak. Read counts in merged peaks were acquired with the "featureCount" function from Rsubread (2.2.6) using alignment output ".bam" files from the nucleosome-free fraction of each sample. Peaks within the previously reported blacklist regions[78] were removed from further analysis (https://github.com/Boyle-Lab/Blacklist/blob/master/lists/mm10-blacklist.v2.bed.gz) (Csnk2a1 TSS was found within the blacklist regions and was isolated for analysis). CHIPseeker (1.28.3) was used to annotate ATAC peaks. Peaks within 1000bp of any transcription start site (TSS) were selected for differential affinity analysis using DESeq2 (1.32.0) with raw counts within selected peaks as inputs. Analysis result is included in Data S2.

Gene set enrichment analysis

RNA-Seq and proteomics data from the mouse colonic epithelium and tumor tissues +/- K-Ras^{G12D} were subjected to gene set enrichment analysis (GSEA). Normalized quantification matrices of RNA and protein were used as inputs. GSEA (4.0.3) desktop application (https://www.gsea-msigdb.org/gsea/index.jsp) was used to run the analysis with the MsigDB Hallmark gene set comparing K-Ras^{G12D} with K-Ras^{WT} tissues. Most default parameters were used with 'Permutation type' set to 'gene_set' due to the small number of phenotype labels. Gene sets with nominal p-value < 0.05 and FDR q-value < 0.1 were considered significant.

Kinase enrichment analysis

Analysis was performed by employing GSEA (4.0.3) on the phospho-proteomic data from the colonic epithelium and tumor +/- K-Ras^{G12D}. Kinase-substrate list that integrated human and mouse phosphorylation sites and their targeting kinase information[79] was used as gene-sets for the analysis.

DepMap analysis

CRISPR gene effect score dataset of the ''DepMap 21Q2 Public+Score, CERES'' release was downloaded from the DepMap portal (https://depmap.org/portal/). Gene effect scores from CRISPR mediated knockout of *AGO2*, *ANKRD52, DICER1, XPO5, TNRC6A, DROSHA*, and *PPP6C* in all cell lines were extracted and plotted.

TCGA analysis

Transcriptomic profile and clinical information of patients with CRC in the TCGA PanCancer Atlas cohort[80] were downloaded from cBioPortal. HEAP target signatures of each patient were calculated using GSVA (1.38.2).[72] Patients with HEAP target signature in the top/bottom 20% of the cohort were selected for survival analysis. To evaluate K-RAS signaling status in patients, we scored patients K-RAS activation using GSVA and the K-RAS_UP gene set from MsigDB. Patients with top/bottom 10% K-RAS activation were selected for survival, differential gene expression, and functional enrichment analysis. Both miRNA target signatures and Hallmark pathway enrichment results for TCGA COAD cohort is included in Data S4.

scRNA-seq analysis

VUMC Discovery Set[58] includes 62 independent scRNA-seq datasets from premalignant tumors. 65,088 epithelial cells were retained after filtering for high-quality barcodes using dropkick.[81]

Data normalization and UMAP visualization

Analysis of scRNA-seq data was performed in Python using scanpy, pandas, and numpy packages as previously described.[58] Briefly, raw scRNA-seq counts were normalized by median library size, log-like transformed with Arcsinh, and Z- score standardized per gene. The Single-Cell rEgulatory Network Inference and Clustering or SCENIC pipeline was used to integrate pre-cancer and their corresponding normal tissue datasets.[82,83] ''scanpy.tl.umap'' function was used to compute UMAP coordinates of the dataset from

the dataset's Z-score standardized AUCell values from SCENIC analysis, its 50-principal component decompositions with no feature selection, and a subsequent KNN graph with k equal to the square root of the number cells projected. Normalized expression of CSNK genes and miRNA target gene scores were overlaid onto UMAPs of the Discovery set and 3 subsets extracted from it based on cell type: Adenoma-Specific Cells (ASC), Serrated-Specific Cells (SSC), and Goblet cells (GOB). KRAS multi-hit status was inquired from somatic mutation called from the Discovery set's whole-exosome sequencing result as previously described[58] and was overlaid onto a UMAP. miRNA target gene scores were computed using 'scanpy.tl.score_genes' function with the full list of miRNA target genes and a control sampling size of 2,000 as inputs to the function.

Scatter plots

Scatter plots between each CSNK gene's expression and the miRNA target scores of ASC, SSC and GOB subsets were visualized using seaborn's 'scatterplot' function. The input data for each CSNK gene's plot was filtered at a threshold from binning the cells based on the specific CSNK gene's expression. The thresholds were chosen such that the cell count from the first bin kept is lower than the last bin excluded by 40% of the sample size to filter out many low-expression cells. Regression lines were fitted using scipy's 'stats.linregress' function, and spearman's rank correlation coefficients and corresponding p-values were computed using scipy's 'stats.spearmanr' function.

Box plots

Gene scores of target genes from each miRNA family were calculated using 'scanpy.tl.score_genes' . For each subset (ASC, SSC and GOB), cells were grouped by their rank of the gene scores calculated from the target genes of all miRNA families. Comparisons of the target gene scores of selected miRNA families between top and bottom 20% populations of cells ranked by the gene score calculated from all miRNA target genes were visualized using seaborn's 'boxplot' function. Two-sided Mann-Whitney-Wilcoxon tests were performed to infer statistical differences between groups.

GSVA

GSVA analysis was performed using GSVA (1.38.2) with the MsigDB Hallmark, C2, and C6 gene set.[72] Differential enrichment analysis using pathway scores from top and bottom 20% of ASCs, SSCs, and GOBs ranked by miRNA target signature were performed using limma (3.52.2).[74] Pathways with adjusted p-value < 0.01 and $|LFC|$ (miRNA signature high cells vs miRNA signature low cells) > 0.4 in all three cell types were considered differentially enriched.